Monitoring the evolution of sulfur isotope and metal concentrations across gold-bearing pyrite of Carlin-type gold deposits in the Youjiang Basin, SW China

Wei Gao [a], Ruizhong Hu [a,b,*], Lu Mei [a,b], Xianwu Bi [a], Shanling Fu [a], Mingliang Huang [a], Jun Yan [a], Jinwei Li [c]

[a] State Key Laboratory of Ore Deposit Geochemistry, Institute of Geochemistry, Chinese Academy of Sciences, Guiyang 550081, China
[b] College of Earth and Planetary Sciences, University of Chinese Academy of Sciences, Beijing 100049, China
[c] Research Center of Ancient Ceramic, Jingdezhen Ceramic University, Jingdezhen 333001, China

ARTICLE INFO

ABSTRACT

The Youjiang Basin in Southwest China is the world's second largest Carlin-type gold (Au)-producing region. However, the source of reduced sulfur that accounts for Au transport in ore-forming fluids remains controversial. Finely characterizing the sulfur isotopic compositions ($\delta^{34}S$ values) in micron-scale zonation of Au-bearing pyrite is the key to clearly identify sulfur source. Here, we used high-resolution nanoscale secondary ion mass spectrometry (Nano-SIMS) to characterize the temporal variation in $\delta^{34}S$ values and its relationship with metal contents across Au-bearing pyrite from the Linwang and Badu deposits in the Youjiang Basin, with the aim of monitoring the source and evolution of reduced sulfur in auriferous fluids. The Au-bearing pyrite rims in the Linwang deposit contain three growth stages that record episodic injections of Au- and As-rich fluids. Within these rims, the $\delta^{34}S$ values vary inversely with Au concentrations. The inner rims with the high Au contents have $\delta^{34}S$ values of -1.7‰ to $+3.3$‰ that are comparable to those of magmatic sulfur. The outer rims with decreasing Au contents have $\delta^{34}S$ values of $+1.3$‰ to $+15.7$‰ that gradually approach those of pre-ore pyrite in the host rock. Such a variation indicates that the reduced sulfur in the initial Au-bearing ore-forming fluids was primarily originated from deep magmatic-hydrothermal systems while the host rock-derived ^{34}S-enriched sulfur increasingly dominated through fluid-rock interactions during mineralization. In contrast, Au-bearing pyrite from the Badu deposit has positive $\delta^{34}S$ values ranging from $+9.0$‰ to $+25.8$‰, which overlap those of diagenetic pyrite in the Devonian sedimentary rocks. Combining the intimate spatial association between Au mineralization and the Devonian strata, we propose that the initial ore-forming fluids have leached substantial sulfur from the Devonian strata. Significant contaminations of sedimentary sulfur erased the primary sulfur isotopic signals of the initial auriferous fluids. Our interpretations of these two deposits may also apply to other Carlin-type Au deposits in the Youjiang Basin, where $\delta^{34}S$ values of Au-bearing pyrite show host rock-dependent variations. This study demonstrates that high-resolution Nano-SIMS sulfur isotope and elemental analysis of Au-bearing pyrite is a potent tool for tracing the source and evolution of reduced sulfur in ore-forming fluids for sedimentary-host Au deposits worldwide.

1. Introduction

Carlin-type gold deposits (CTGDs) are one of the most important types of hydrothermal Au deposits, with prime examples found in Nevada, USA, and the Youjiang Basin, Southwest China. These two regions are endowed with approximately 8000 and 1000 tons of Au, respectively, accounting for 6 % of annual global Au production (Cline et al., 2005, 2013; Hu et al., 2017, 2020a; Muntean and Cline, 2018). The characteristics of CTGDs have been well-established after decades of extensive attentions from economic geologists and mining companies, as reviewed by Hofstra and Cline. (2000), Hu et al. (2002, 2017), Cline et al. (2005), Muntean and Cline. (2018), Cline. (2018) and Su et al. (2018). However, the ultimate sources of ore-forming components (fluids, reduced sulfur, and metals) remain highly debated partly due to

---

the fine-grained nature of ore minerals and the complex evolution of auriferous fluids from their source to the final site of mineralization. Suggested candidates include sedimentary strata leached by deep-circulating meteoric water or basinal fluids (Hofstra et al., 1999; Emsbo et al., 1999; Hu et al., 2002; Emsbo and Hofstra, 2003; Tosdal et al., 2003; Gu et al., 2012), metamorphic dehydration of black shale hosts or deep crustal rocks (Cline and Hofstra, 2000; Cline et al., 2005; Large et al., 2009, 2011; Su et al., 2009, Su et al., 2018), and deep magmatic-hydrothermal systems (Kesler et al., 2005; Barker et al., 2009; Muntean et al., 2011; Large et al., 2016; Xie et al., 2018; Jin et al., 2020).

Gold is predominantly transported as hydrosulfide complexes in ore-forming fluids of Carlin-type Au mineralization systems [$Au(HS)_2^-$ and $AuHS$; Simon et al., 1999; Williams-Jones et al., 2009; Pokrovski et al., 2014], and then incorporated into the lattice of arsenian pyrite as 'invisible' forms (Simon et al., 1999; Palenik et al., 2004; Reich et al., 2005; Su et al., 2012). Thus, monitoring the change in sulfur isotope compositions ($\delta^{34}S$) and its relationship with metal contents across arsenian pyrite could advance our understanding of the source and evolution of reduced sulfur in auriferous fluids (Kesler et al., 2005; Barker et al., 2009; LaFlamme et al., 2018). However, Au-bearing pyrite in CTGDs commonly contains a core-rim texture with Au-bearing rim having oscillatory zoning of micron-scale (Hu et al., 2002, 2017; Barker et al., 2009; Su et al., 2012, 2018; Xie et al., 2018; Yan et al., 2018; Li et al., 2020). Conventional bulk isotope analyses often result in geologically equivocal interpretations. In-situ analysis of laser ablation-multicollectorinductively coupled plasma-mass spectrometry (LA-MC-ICP-MS) also is compromised by its large spot size (tens of microns at best) that encompasses multiple zones with different isotope and elemental compositions. In contrast, nanoscale secondary ion mass spectrometry (Nano-SIMS) has the advantages of sub-100 nm spatial resolution and low detection limits and can contemporaneously obtain precise $\delta^{34}S$ values and qualitative mapping of trace elements with low concentrations. Therefore, it can effectively reveal the variations in sulfur isotope composition and metal content across Au-bearing pyrite rims of CTGDs (Barker et al., 2009; Yan et al., 2018; Li et al., 2020; Gopon et al., 2020).

In this study, we conducted *in-situ* high-resolution Nano-SIMS analyses to characterize the variation in $\delta^{34}S$ values and its relationship with Au contents across arsenian pyrite from the Linwang and Badu CTGDs in the Youjiang Basin, aiming to trace the source and evolution of reduced sulfur in ore-forming fluids. We then recompiled all reported *in-situ* $\delta^{34}S$ data of Au-bearing pyrite from 11 CTGDs throughout the Youjiang Basin to reconcile the disparities in previous studies and fingerprint the source of reduced sulfur in auriferous fluids at a basinal scale.

2. Regional geology

The South China Block comprises the Yangtze and Cathaysia Blocks, which were welded together at ca. 830 Ma (Fig. 1a, Zhao et al., 2011). It was rifted from the Gondwana Continent during the early Devonian due to opening of the Paleo-Tethys (Metcalfe, 2006). Following subduction and progressive closure of the Paleo-Tethys, the collisions between the South China and Indochina Blocks and between the South China Block and North China Craton during the Triassic formed the Song Ma suture zone to the south and the Qinling-Dabie Orogenic Belt to the north, respectively (Wang et al., 2013).
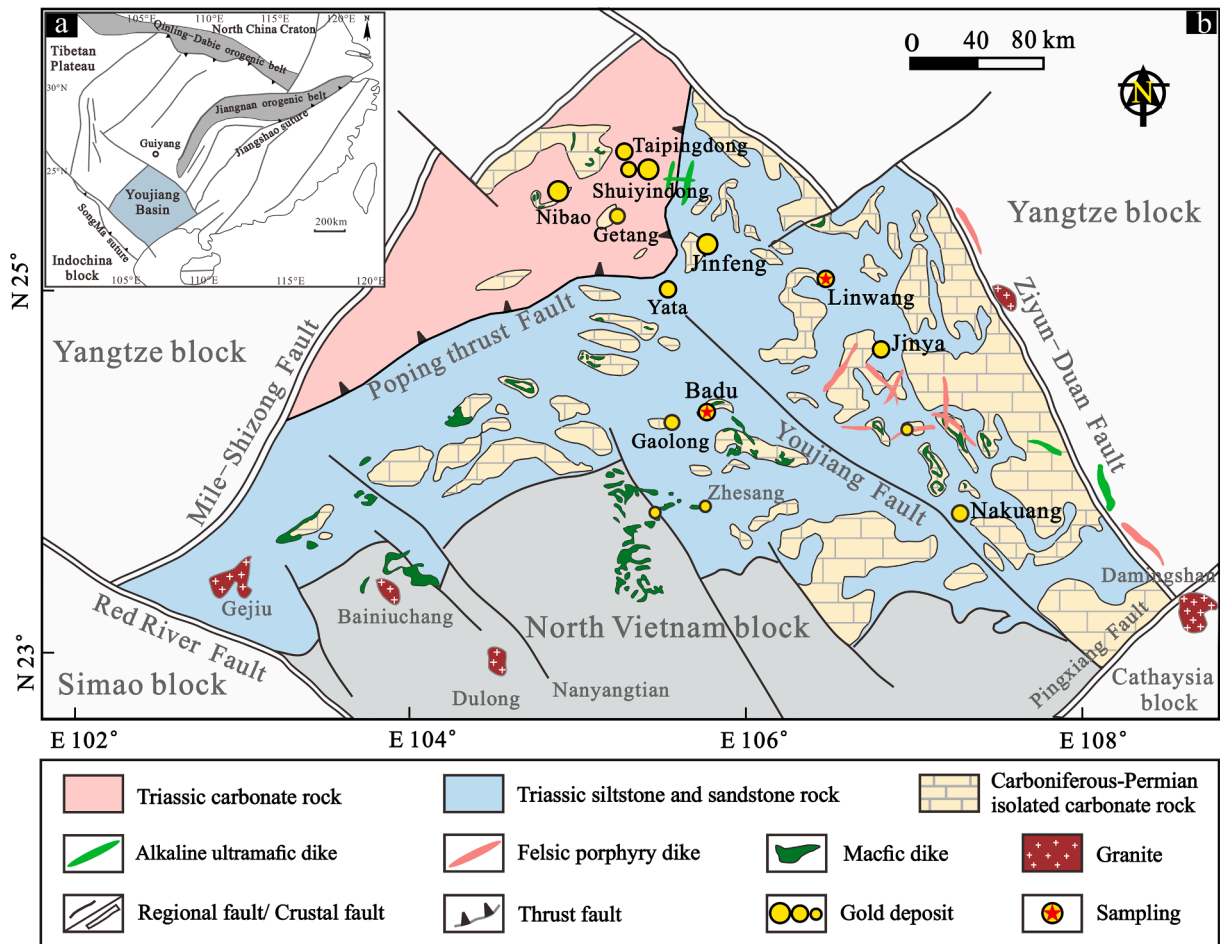

Fig. 1. (a) A simplified tectonic map of the South China Block and adjacent regions showing the location of the Youjiang Basin. (b) A geologic map of the Youjiang Basin showing the distribution of representative Carlin-type Au deposits (modified from Gao et al., 2021).

The Youjiang Basin is located at the southwestern margin of the Yangtze Block and extends from Southwest China to North Vietnam (Fig. 1b). It is a diamond-shaped sedimentary basin bounded by a series of NE- and NW-striking basement-penetrating faults, including the Mile-Shizong, Ziyun-Yadu, Pingxiang-Nanning and Redriver-Ailaoshan faults in the northwest, northeast, southeast, and southwest, respectively (Hu and Zhou 2012; Hu et al. 2017). Several important faults occur within the basin like the NW-trending Youjiang and NE-trending Poping faults (Fig. 1b). The Youjiang Basin experienced three evolution stages: an early Devonian to early Permian rifting basin, late Permian back-arc basin, and Middle-Late Triassic foreland basin during the opening, subduction, and closure of the Paleo-Tethys and the subsequent collision between the South China and the Indochina Blocks (Du et al., 2009, 2013; Yan et al., 2006; Cai and Zhang, 2009; Yang et al., 2012). During the Late Jurassic to Early Cretaceous, subduction of the Paleo-Pacific plate beneath South China resulted in top-to-the-NW thrusting and fault-propagation folding, which superposed on the Triassic NW-trending structures within the basin (Qiu et al., 2016).

The basin is filled with over 7-km-thick marine sedimentary successions of the Cambrian to Middle Triassic periods (Song et al. 2009; Hu et al. 2017). The Cambrian and Ordovician strata are locally exposed in some anticline cores. Geographically, a sequence of shallow-water carbonate platforms was deposited in the northwestern part of the basin during the Devonian to Triassic. In contrast, a sequence of deep-water slope/basin calcareous sandstone, siltstone, and shale was deposited in the southeastern part of the basin (Fig. 1b, Du et al. 2013). Sedimentary strata in the basin only expeienced low-grade burial metamorphism (Suo et al. 1998).

Some igneous rocks, mainly basalts, dolerites, and minor felsic dikes and andesites, are locally exposed within the basin (Fig. 1b). Geochronological data suggest that they dominantly formed at ca. ~ 260, 230–205, 160–155, and 100–84 Ma (Gao et al., 2021, and reference therein). Some ca. 100–80 Ma S-type granites and related W-Sn polymetallic deposits occur at the southern and eastern margins of the basin (Cheng et al., 2009, 2010; Feng et al., 2010). Additionally, inherited zircons collected from felsic dikes with ages of 100–94 Ma in the center and south of the basin yielded U-Pb ages of 145–130 Ma, suggesting deep contemporaneous hidden intrusions (Zhu et al., 2016; Gao, 2018).

The Youjiang Basin hosts more than 200 CTGDs with updated Au reserves of nearly 1000 tons (Hu et al., 2020a), making it the world's second largest Carlin-type Au province after Nevada (Hu et al., 2017; Su et al., 2018). Gold mineralization is clustered along regional NE- and NW-striking faults and mainly occurs within the late Permian bioclastic limestone and Middle Triassic siltstone and mudstone, both of which contain abundant Fe-bearing carbonate minerals (Hu et al., 2017). Some deposits are also variably hosted by the Cambrian, Devonian, and Carbonaceous strata. Additionally, a few deposits in the southern part of the basin occur within altered dolerite (Gao et al., 2021). Gold mineralization in all deposits was stratigraphically and structurally controlled. In addition to the well-known Shuiyindong and Jinfeng deposits, Linwang and Badu are two representative large Au deposits in the basin.

3. Deposit Geology

3.1. The Linwang deposit

The Linwang deposit, having proven Au reserves of more than 30 t (0.97 Moz) with an average grade of 5 g/t (0.19 oz/t), is located at the northeastern margin of the Leye platform carbonates. Strata exposed in the Linwang district comprise three sequences (Chen et al., 2010). Isolated platform carbonates, exposed in the western part of the district, are dominated by carbonates of the Permian Maokou and Heshan formations, and thin-bedded limestone with interlayered mudstone of the Lower Triassic Luolou Formation. Moving east, shelf-facies sedimentary rocks comprise calcareous mudstone intercalated with silty mudstone of the Middle Triassic Banna Formation. Further east, basin-facies

sedimentary rocks are primarily composed of terrestrial clastic turbidite of the Middle Triassic Baifeng Formation. No igneous rocks have been identified in ore districts by geological mapping or drilling. The nearest igneous rocks are the NW-trending Jiayou and NE-trending Naling felsic dikes, approximately 80 km from the Linwang deposit.

Gold mineralization is mainly hosted within subunit 1 of the fourth unit of the Baifeng Formation (unit 4–1 of the Baifeng Formation, Fig. 2). Unit 4–1 includes five layers (4-1a to 4-1e). Unit 4-1a is composed of mudstone, silty mudstone, and siltstone, with pyrite nodules. Unit 4-1b is calcareous siltstone with interlayered mudstone. Unit 4-1c is composed of mudstone and pelitic siltstone. Unit 4-1d consists of calcareous quartz sandstone with intercalated siltstone and mudstone. Unit 4-1e comprise mudstone and silty mudstone. Gold mineralization occurs as veins and lenses hosted within calcareous sandstone, siltstone, and silty mudstone of the units 4-1a to 4-1c, and is structurally controlled by secondary faults between the south-north trending F_7 and F_1 faults (Fig. 2). The deposit is divided into three ore blocks from north to south: Baan, Kuangshan and Shanmulin. The Kuangshan block contributes 72 % of the Au reverses, and includes eight orebodies.

Detailed petrographic examination of sample transects that covered barren and mineralized rocks with different Au grades were conducted to reveal the alteration features associated with Au mineralization. The barren host rocks are dolomitic calcareous siltstones that contain abundant Fe-bearing dolomite, quartz, minor dolomite and calcite, and trace muscovite and sulfides (Fig. 4a-b). Fe-bearing dolomite has irregular and zigzag margins, and encloses mineral inclusions of quartz, muscovite, and sulfides with similar characteristics to those in the surrounding clastic matrix.
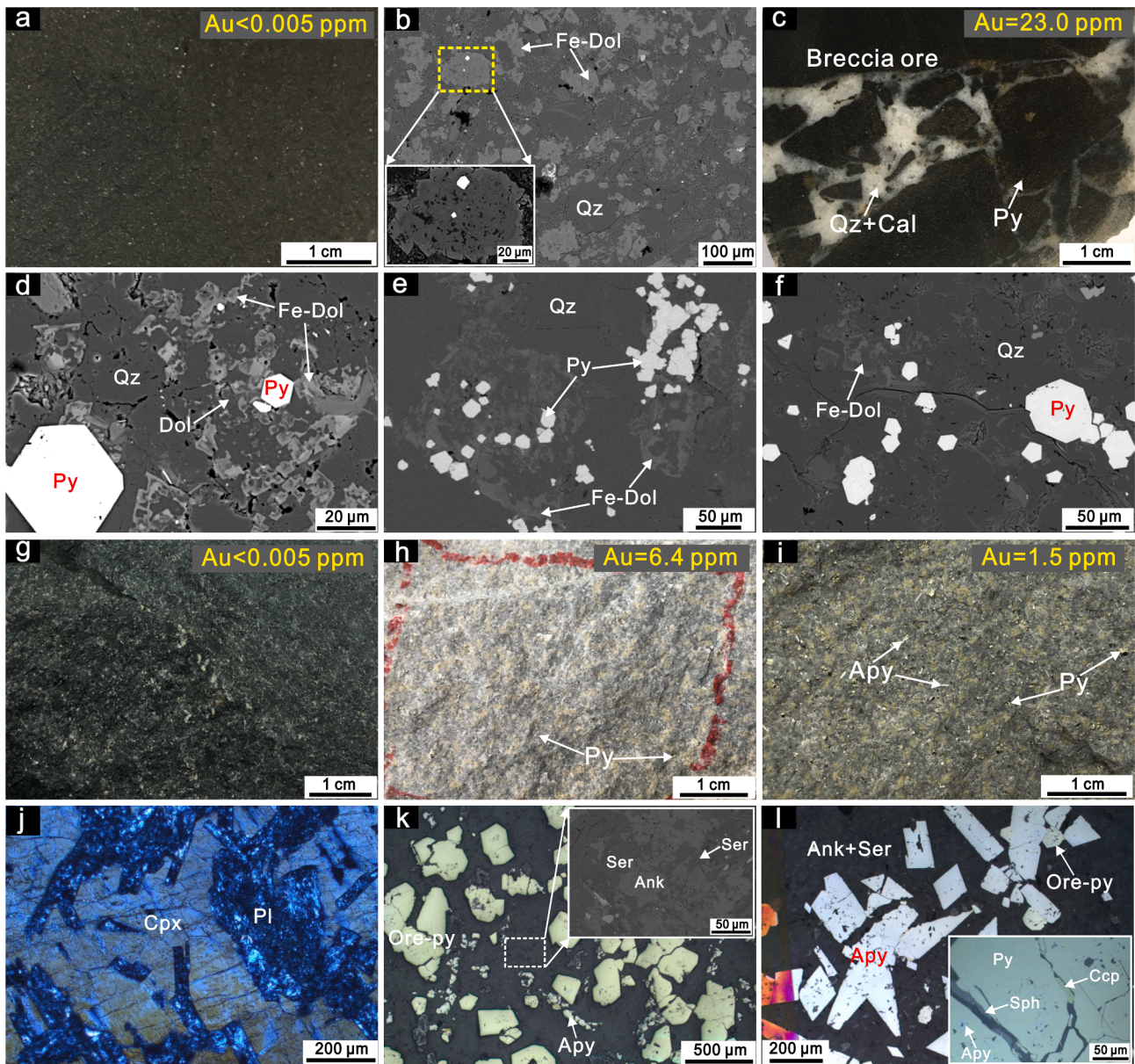
In the mineralized samples, Fe-bearing dolomite is obviously decreased. Hydrothermal quartz gradually penetrated and replaced Fe-bearing dolomite (Fig. 4d-f). This newly formed quartz contains residual tiny inclusions of Fe-bearing dolomite, indicating decarbonation (Su et al., 2009). In addition, Fe-bearing dolomite was altered to Fe-barren dolomite enclosed by hydrothermal quartz. These processes locally preserved the morphology of Fe-bearing dolomite (Fig. 4e). In high-grade samples, Fe-bearing dolomite was almost completely replaced by hydrothermal quartz, resulting in intensive silicification (Fig. 4f). Accompanying decarbonation and silicification, Fe released from Fe-bearing dolomite was sulfidized to form hydrothermal pyrite. Pyrite grains show a consistent spatial association with hydrothermal quartz and dolomite (Fig. 4d-e), where they are distributed along the boundaries of, or disseminated within, hydrothermal quartz, suggesting that they were nearly contemporaneous.

Stibnite, realgar, orpiment, calcite, and minor quartz, constitute the late-stage minerals, representing the cooling of hydrothermal systems (Cline et al., 2005; Xie et al., 2018). Stibnite occurs as euhedral crystals in open spaces together with drusy quartz or calcite. Realgar and orpiment commonly occur as fillings along the fractures of ore-stage quartz veinlets, or as veinlets crosscutting previously mineralized samples.

3.2. The Badu deposit

The Badu deposit is the largest dolerite-hosted Au deposit in the Youjiang Basin, with estimated Au reserves of 35 t (Jinfeng Corporation, 2018). The detailed geology of Badu was described by Gao et al. (2021), and the key characteristics are summarized here. The deposit is located on the western flank of the Badu anticline, which has the core of the Devonian rocks and rims of the Permian to Middle Triassic sequences (Fig. 3). The anticline is crosscut by numerous NE- and NW-trending faults that formed simultaneously with folding and deformation. The strata exposed in the ore district includes the Yujiang Formation mudstone and siltstone (D_1y), Liujiang Formation chert interbedded with tuff and lenses of banded limestone (D_3l), Carboniferous mudstone and chert, Sidazhai Formation limestone ($P_{1-2}sd$), Linghao Formation mudstone, argillaceous sandstone and tuff ($P_{2-3}lh$), and sandstone, siltstone, and mudstone of the Shipao and Baifeng formations (T_1s and

Fig. 2. Schematic geologic map (a) and two representative geologic cross sections (b) of the Linwang deposit (modified from Chen et al., 2010).

Fig. 3. Schematic geologic map (a) and representative geologic cross section of the dolerite-hosted No. Vl orebody (b) of the Badu deposit (modified from Gao et al., 2021).

T_2bf). Numerous dolerite dikes were predominantly intruded the Devonian to Permian sedimentary strata along NE- and NW-trending faults. Early 1:50,000-scale geological mapping divided the dolerites into three stages (BGMRGX, 1992).

Gold mineralization in Badu includes seven major orebodies with vein- or tabular- shapes (Fig. 3), which are spatially controlled by NE-striking secondary faults. Orebodies I and II are hosted by mudstone and siltstone of the Lower Devonian Yujiang Formation. Orebodies No. III to VII mainly occur within hydrothermally altered dolerites that are fractured by fault zones, or occur along faulted contacts between dolerite and sedimentary strata. Each orebody is composed of a series of veins, and each mineralized vein extends from 10 to 500 m along strike,

varies in thickness from 2 to 50 m, and extends vertically below the surface by up to ~ 200 m. Orebodies VI and VII are the most representative dolerite-hosted orebodies in the ore district, with Au grades varying from 1 to 20 g/t (Gao et al. 2021).

The fresh dolerite is greyish-green in color (Fig. 4g), and dominantly composed of magmatic plagioclase and clinopyroxene, which show typical poikilophitic textures (Fig. 4j). Iron-titanium oxides and apatite are major accessory minerals. The altered and mineralized dolerite is distinguished by its bleached appearance and occurrence of abundant disseminated pyrite and arsenopyrite (Fig. 4h-i). The amounts and relative proportions of pyrite and arsenopyrite are spatially variable. Pyrite is the predominant ore mineral in the richest orebody VI (Fig. 4h),

Fig. 4. Photographs and photomicrographs of variably altered and mineralized samples from the Linwang (a-f) and Badu (g-l) deposits showing the alteration features associated with gold mineralization. (a-b) Unaltered calcareous siltstone containing abundant ferroan dolomite with mineral inclusions of clastic matrix. (c) High-grade brecciated siltstone with intense silicification and abundant disseminated pyrite. (d-f) Variably altered and mineralized samples showing that ferroan dolomite were gradually dissolved and replaced by hydrothermal quartz, which was accompanied by the formation of gold-bearing pyrite. (g, j) Least altered dolerite with porphyritic texture. (h, k) Mineralized dolerite with intermediate gold grade containing abundant pyrite. (i, l) Mineralized dolerite with low gold grade containing nearly equivalent pyrite and arsenopyrite. (a, c, g-i) Hand specimens. (b, d-f) BSE image. (j) Crossed-polarized light. (k-l) Reflected light. Abbreviations: Ank = ankerite, Apy = arsenopyrite, Cal = calcite, Ccp = chalcopyrite, Cpx = clinopyroxene, Dol = dolomite, Fe-Dol = Fe-bearing dolomite, Pl = plagioclase, Py = pyrite, Qz = quartz, Ser = sericite, Sph = sphalerite.

but arsenopyrite and pyrite are equivalent in the orebody VII with low gold grades (Fig. 4i). In addition, mineralized dolerite is characterized by milky quartz veins that enclose elongated and irregular fragments of mineralized dolerite. However, quartz veins do not contain any significant sulfides and are thus not mineralized.

Petrographic observations show that the primary magmatic minerals have been completely altered to ankerite, sericite, pyrite, arsenopyrite, rutile, minor base metal sulfides, apatite, and trace monazite during mineralization (Fig. 4k). On the basis of macro- and micro-textural relationships, three principal stages of alteration and mineralization can be identified (Gao et al., 2021). The stage 1 is characterized by the ubiquitous formation of ankerite, sericite, and rutile as a result of alterations of magmatic pyroxene, plagioclase, and iron–titanium oxides.

Ankerite and sericite preserve pseudomorphs of the primary poikilophitic textures (Fig. 4k). Hydrothermal rutile formed by the breakdown and pseudomorphic replacement of magmatic ilmenite (Gao et al., 2021). The stage 2 is characterized by sulfidation, which formed pyrite and arsenopyrite disseminated in the matrix of ankerite and sericite. Pyrite crystals generally contain inclusions of minerals formed in the stage 1. The stage 2 also formed quartz veinlets that locally enclose ore-stage pyrite and arsenopyrite, suggesting that these veinlets were synchronous with, or slightly later than, sulfidation. Some later Cu-Zn-Sb sulfides, mainly including chalcopyrite, sphalerite, tetrahedrite, and stibnite, occur as strings or fillings along microfractures in pyrite (Fig. 4l). The stage 3 formed quartz-carbonate veins crosscutting mineralized dolerite and ore-stage quartz veinlets. Trace amounts of

stibnite and realgar crystals filled the open spaces. Locally, coarse-grained barite occurs as veinlets crosscutting all the previous stages (Dong, 2017).

Geochronological data suggest that the dolerite hosts were emplaced at ca. ~ 212 Ma, but Au mineralization occurred at ca. ~ 144 Ma, synchronous with other sedimentary-hosted CTGDs in the Youjiang basin (Gao et al., 2021).

3.3. Sampling and analytical methods

The Linwang and Badu deposits are representative of two types of CTGDs in the Youjiang basin: sedimentary-hosted and dolerite-hosted, respectively. A series of host rocks and mineralized samples with various Au grades and degrees of alteration were taken from outcrops, open pits and drill holes. Representative host rocks and mineralized samples were prepared as standard thin sections. Optical microscopy and scanning electron microscope with backscattered electron imaging (SEM-BSE) were used to determine the hydrothermal alteration, mineral paragenesis, and various types of pyrite. The internal texture and zoning of pyrite were characterized using high-contrast BSE imaging. The interested areas containing the most typical pyrite grains were carefully drilled out as discs with 5 ~ 25 mm in diameter. All discs were then re-examined and photomicrographed using reflected light and SEM to precisely navigate and locate the pyrite grains of interest.

In-situ sulfur isotope and elemental mapping analyses of selected pyrite grains were conducted using a CAMECA Nano-SIMS 50L at the Institute of Geology and Geophysics, Chinese Academy of Sciences, Beijing, following previous methods (Zhang et al., 2014; Yan et al., 2018). Briefly, a primary Cs^+ ion beam of 1–2 pA and 100 nm in diameter was used for both types of analyses. ^{32}S was counted using Faraday cup to avoid the quasi-simultaneous arrival effect, and ^{34}S and other elements were counted using electronic multipliers. Certified international standards (CAR-123 pyrite) and internal reference samples (PY-1117 and CS01 pyrites) were used during the analysis. Instrumental mass fractionation was corrected using the sample-standard bracketing method. The total count time for each analysis was 150 s, consisting of 300 cycles of 0.5 s. The spots were approximately 2 × 2 μm in size. The analytical precision (1σ) was about ± 0.5 per mil. The secondary electrons of ^{34}S, $^{75}As^{32}S$, $^{197}Au^{32}S$, $^{63}Cu^{32}S$, $^{121}Sb^{32}S$, and $^{208}Pb^{32}S$ were used for elemental mapping. The peaks were calibrated using working references of arsenopyrite (^{75}As), Au foil (^{197}Au), chalcopyrite ($^{63}Cu^{32}S$), SbS_2 (^{121}Sb) and galena ($^{208}Pb^{32}S$). A mass resolution of ca. 9000 (at 10 % peak height) was used to eliminate the isobaric interferences. Mapping images had a size of 25 × 25 μm or 50 × 50 μm with a corresponding resolution of 256 × 256 or 512 × 512 pixels, respectively. Generally, the color scales of the collected images only provide the relative signal intensities of different elements, and do not represent their absolute contents, which means that different images are not comparable in the scales of signal intensities.
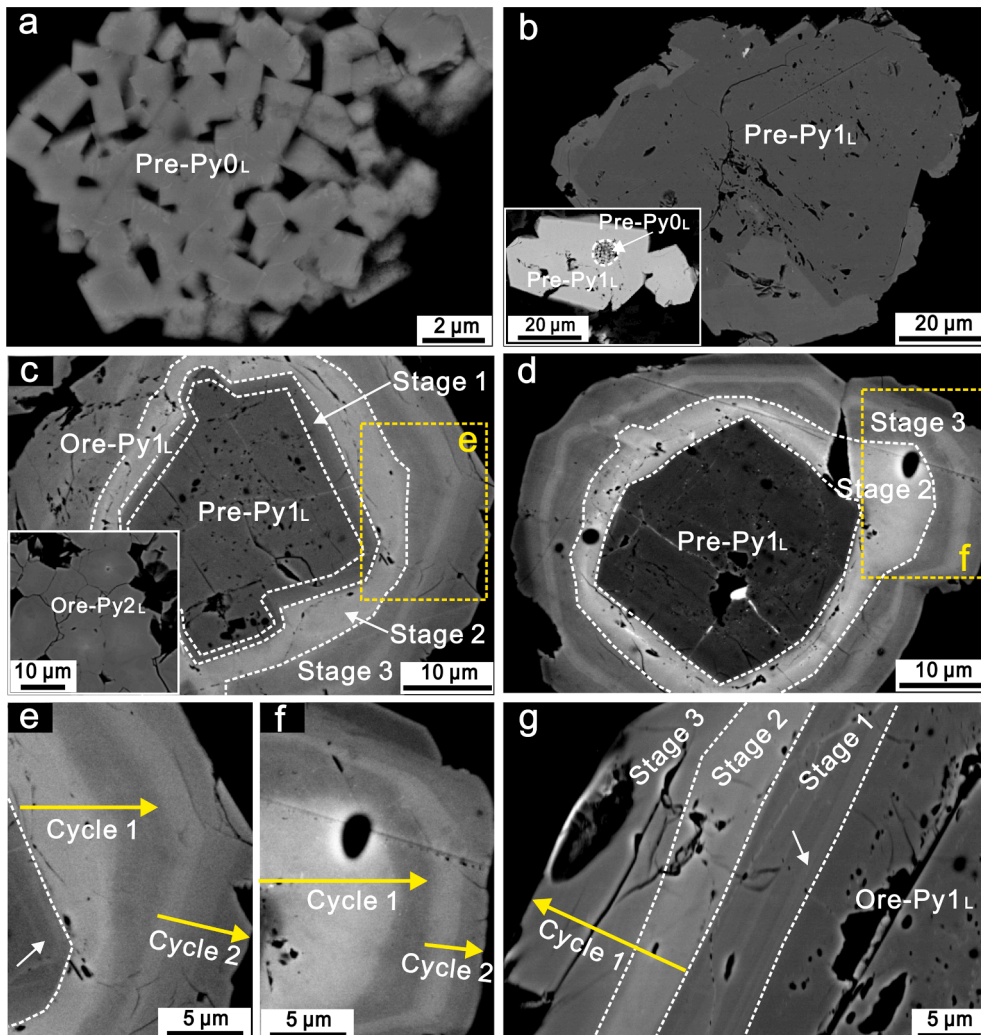
Fig. 5. BSE images of various pyrite types from the Linwang deposit. (a) Pre-ore framboidal pyrite (Pre-Py0$_L$) in barren samples. (b) Pre-ore anhedral to euhedral pyrite with abundant mineral inclusions and pores (Pre-Py1$_L$) in barren samples, which locally enclose Pre-Py0$_L$. (c-d) Pyrite with core-rim textures in mineralized samples. The core is resemble to Pre-Py1$_L$ in barren samples, but the rim (Ore-Py1$_L$) formed during gold mineralization and displays three growth stages. Ore pyrite also formed individual fine-grained aggregate (Ore-Py2$_L$) without pre-ore core. (e-g) Cycled variations of As contents in the stage 2 and stage 3 pyrite rims. (e) and (f) are enlarged images of yellow frames from (c) and (d), respectively. Abbreviations: Ore-Py = ore pyrite, Pre-Py = preore pyrite. (For interpretation of the references to color in this figure legend, the reader is referred to the web version of this article.)

4. Results

4.1. Pyrite types and paragenesis

Five major types of pyrite were recognized in both the Linwang and Badu deposits, including pre-ore pyrites (Pre-Py0$_L$ and Pre-Py1$_L$ for Linwang, and Pre-Py$_B$ for Badu) and ore pyrites (Ore-Py1$_L$ and Ore-Py2$_L$ for Linwang, and Ore-Py1$_B$ to Ore-Py4$_B$ for Badu), respectively. These pyrites show different occurrence, morphology, and internal texture.

4.2. Linwang deposit

Two types of pyrite were recognized in the barren host rocks of the Linwang deposit: Pre-Py0$_L$ and Pre-Py1$_L$. Pre-Py0$_L$ is framboidal pyrite composed of cubic crystallites less than 2 μm in diameter (Fig. 5a), which is not the focuss of the following analyses. Pre-Py1$_L$ either occurs as anhedral to euhedral independent grains in the barren samples (Fig. 5b), or forms anhedral cores overgrown by ore pyrite rims in the mineralized samples (Fig. 5c-d). It contains abundant mineral inclusions and pores, and is locally observed to enclose Pre-Py0$_L$ (Fig. 5b). Occasionally, Pre-Py1$_L$ grains have bright rims that contain elevated As over 1.0 wt%.

Ore-stage pyrites in mineralized samples occur either as subhedral to euhedral rims (Ore-Py1$_L$) overgrowing pre-ore pyrite cores (Fig. 5c-d), or as small individual fine-grained crystals or aggregates (Ore-Py2$_L$) without pre-ore cores (Fig. 5c). High-contrast BSE imaging shows that

Ore-Py1$_L$ has complex compositional zoning with variable brightness, forming rhythmic alternations of As-higher and As-lower bands. On the basis of brightness and As content, Ore-Py1$_L$ comprises three growth stages (Fig. 5c-d): a relatively dark stage 1 with lower As, a bright stage 2 with the highest As, and stage 3 with intermediate brightness and As content. However, the stage 1 is not always present in all pyrite grains (Fig. 5d). Subtle sub-bands observed at a submicron to nanometer scale are also visible within each stage (e.g., the stage 1 in Fig. 5e and g).

Specifically, the stage 3 commonly recorded a new incursion of As-rich fluids, which together with the stage 2 constitute two repeated cycles of As variation that gradually decreased outwards (Fig. 5e-f). Compared with the stage 2, these renewed As-rich sub-bands are darker. However, Au-bearing rims of some grains only recorded one cycle of As variation (Fig. 5g). Fine-grained individual Ore-Py2$_L$ grains contain As-higher cores and As-lower rims, resembling the stages 2 and 3 of Ore-Py1$_L$.

4.3. Badu deposit

In the Badu deposit, a few fine-grained Pre-Py$_B$ grains were observed in the fresh dolerite, where they mainly occur along the boundaries of, or as dotted grains within, magmatic iron–titanium oxides (Fig. 6a).

Ore-stage pyrites in the mineralized samples show various textures. Ore-Py1$_B$ has anhedral and irregular grain boundaries, and encloses randomly oriented inclusions of early-stage alteration minerals, e.g., ankerite, sericite, and rutile (Fig. 6b-c), suggesting that Ore-Py1$_B$ is of
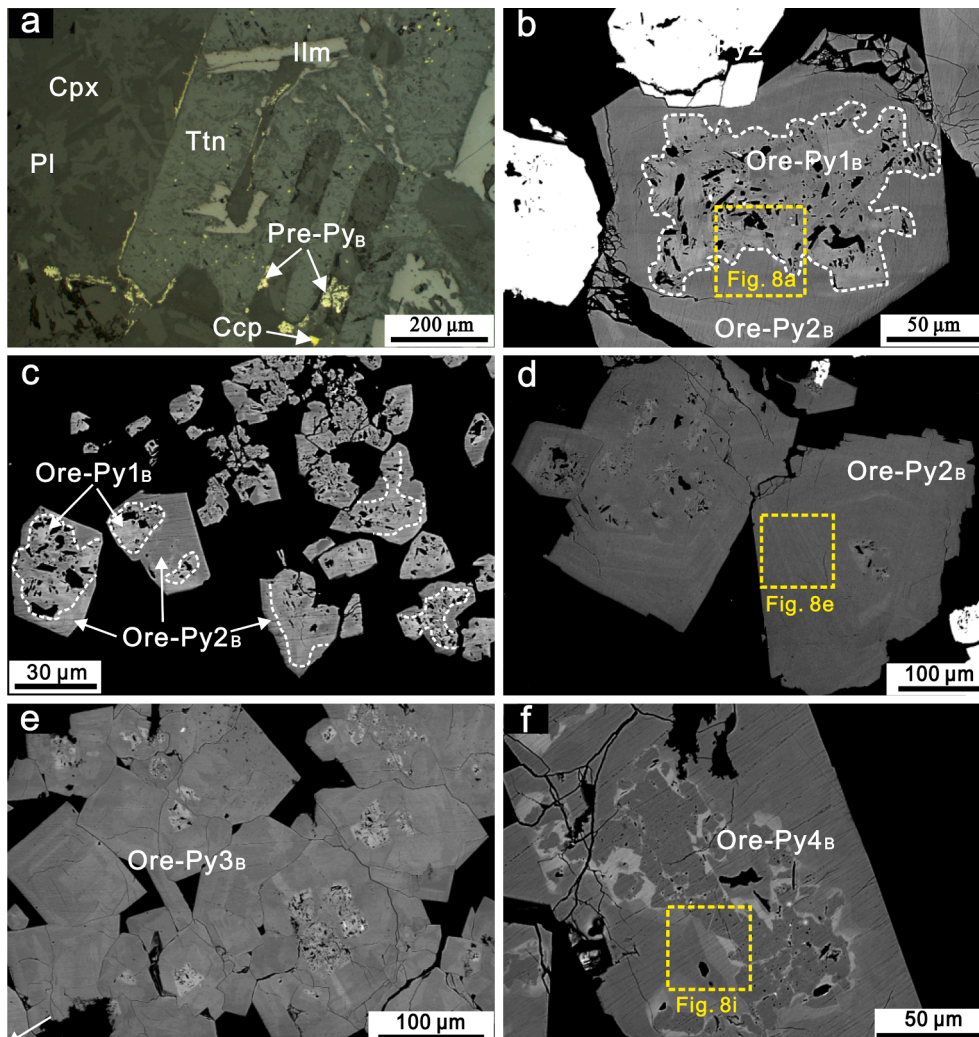
Fig. 6. BSE images of various pyrite types from the Badu deposit. (a) Pre-ore fine-grained pyrite associated with magmatic iron–titanium oxides (Pre-Py$_B$) in barren dolerite. (b-d) Ore pyrite consisting of inclusion-rich core (Ore-Py1$_B$) and clean rim (Ore-Py2$_B$). The mineral inclusions enclosed within Ore-Py1$_B$ are ankerite, sericite, and rutile. (e) Recrystallized ore pyrite (Ore-Py3$_B$) showing patchy zonings of As. (f) Hydrothermally altered ore pyrite (Ore-Py4$_B$) by later fluids, which is characterized by complex microstructure with abundant porosity. Abbreviations: Ccp = chalcopyrite, Cpx = clinopyroxene, Ilm = ilmenite, Pl = plagioclase, Ore-Py = ore pyrite, Pre-Py = preore, Ttn = titanite.

hydrothermal origin. Locally, Ore-Py1$_B$ occurs around, and then gradually replaces, the intergrowths of rutile, ankerite, and sericite, indicating that it formed slightly later than these altered minerals (Gao et al., 2021). Ore-Py1$_B$ contains higher As concentrations, as shown by the lighter response of BSE images. Ore-Py2$_B$ occurs either as clean rims with rare or no mineral inclusions overgrowing Ore-Py1$_B$ (Fig. 6b-c), or as euhedral to subhedral grains disseminated in the matrix of ankerite and sericite (Fig. 6d). Under high-contrast BSE imaging, Ore-Py2$_B$ exhibits rhythmic alternations of thin As-higher and As-lower bands.

Ore-Py3$_B$ commonly forms aggregates and is characterized by patchy zoning of As (Fig. 6e), indicating that it had undergone recrystallization to some degree. However, the primary inclusion-rich Ore-Py1$_B$ and oscillatory zoning of Ore-Py2$_B$ are locally preserved. Ore-Py4$_B$ is secondary altered pyrite that occurs as irregular patchy and porous domains crosscutting the growth zoning of primary pyrite and is characterized by complex internal microstructure with abundant porosity (Fig. 6f). Such textures indicate that Ore-Py4$_B$ is a replacement product of the Ore-Py1$_B$ to Ore-Py3$_B$.
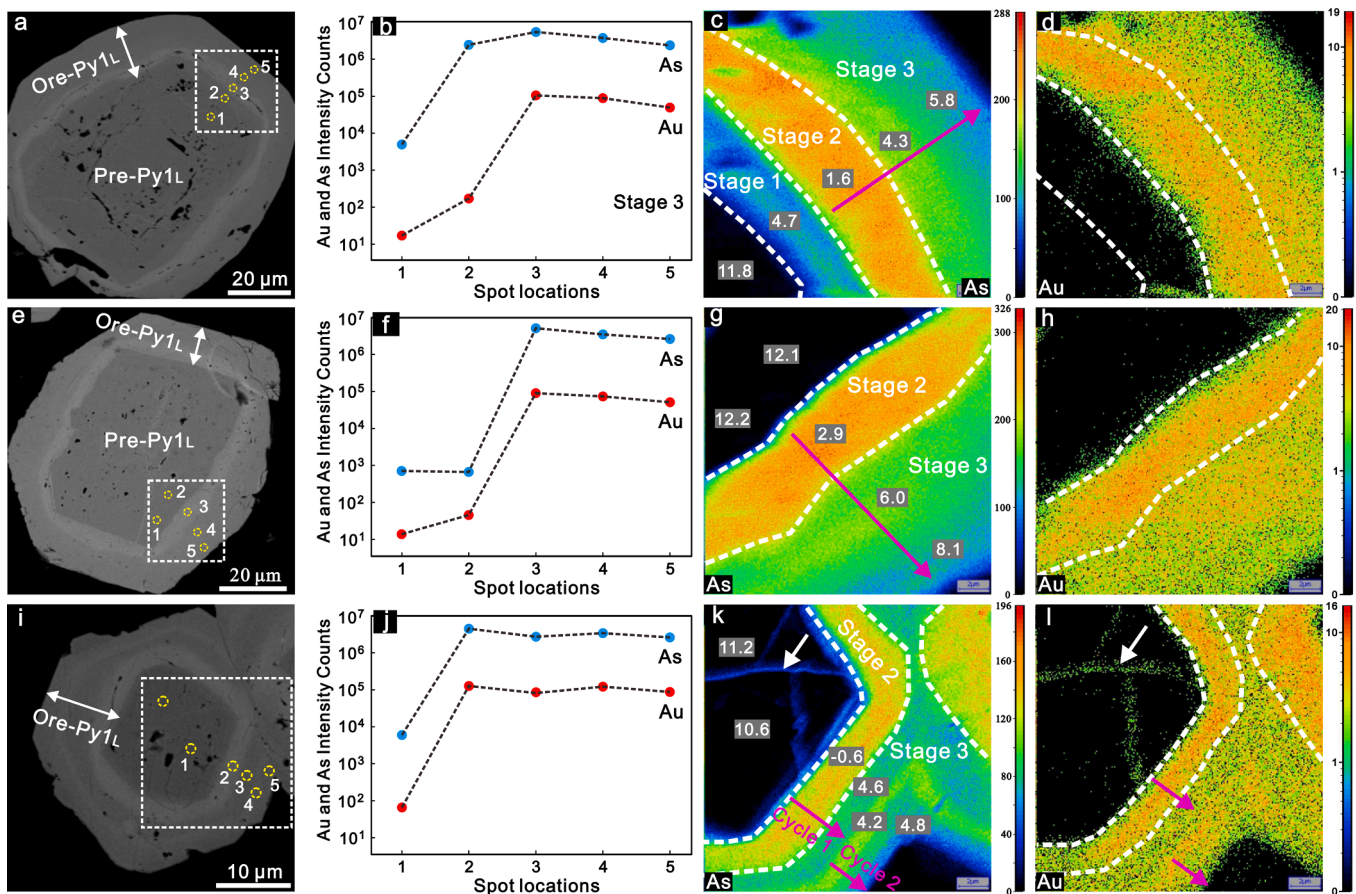
4.4. Nano-SIMS mapping

Representative nano-SIMS mapping results for Au-bearing pyrite grains from the Linwang and Badu deposits are shown in Figures 7 and 8, respectively. For Linwang, pyrite grains with core-rim textures exhibit sharp and distinctive grain-scale distributions of As, Au, and other metals. Pre-Py1$_L$ contains extremely low As, Au, and Cu contents, confirming that it is correctly classified as the pre-ore stage. In contrast, Ore-

Py1$_L$ is characterized by markedly elevated As, Au, and Cu contents. In particular, the three growth stages of Ore-Py1$_L$ show different metal associations and concentrational intensities. The stage 1 shows elevated As and Cu concentrations, but not Au (Fig. 7b-d). The stage 2 contains the highest As and Au contents. The stage 3 has intermediate As, Au, and Cu concentrations that gradually decreased outwards (Fig. 7b-d and f-h). For the grains with two cycles of As variation, the new injection of As-rich fluids was accompanied by an increase in Au contents (Fig. 7j-l). Additionally, some cauliflower-like strings of the stages 2 and 3 with elevated As and Au contents have penetrated and crosscut Pre-Py1$_L$.

For Badu, Pre-Py$_B$ contains little Au and As. The inclusion-rich Ore-Py1$_B$ has higher As and Au contents than those of clean Ore-Py2$_B$ (Fig. 8b-d), further suggesting that it formed during the main Au mineralization. However, the rhythmic zoning of Ore-Py2$_B$ shows positive correlations between As and Au contents, with the bright zoning having elevated As and Au contents that are comparable to Ore-Py1$_B$ (Fig. 8f-h). In contrast, the secondary recrystallized Ore-Py3$_B$ and altered Ore-Py4$_B$ display heterogeneous and complex distributions of As and Au contents, with the brighter domains yielding the higher contents (Fig. 8k-l).

### 4.5. Sulfur isotopic compositions ($\delta^{34}S$) of pyrite at Linwang and Badu

The $\delta^{34}S$ values of 144 Linwang and 105 Badu pyrite analyses are provided in Appendix Tables A1 and A2, respectively, and are summarized in Figs. 9 and 10. For Linwang, the $\delta^{34}S$ values of As- and Au-depleted Pre-Py1$_L$ range from +8.4‰ to +13.8‰ with an average of

Fig. 7. Nano-SIMS elements mapping of representative Au-bearing pyrite grains from the Linwang deposit. (a, e, i) BSE images of analyzed pyrite. The dashed boxes are areas of elements mapping. (b, f, j) Relative intensity counts of Au and As contents, which are contemporaneously obtained during sulfur isotope analyses. The points are labeled in BSE images. (c-d, g-h, k-l) Mappings of Au and As contents. The numbers in c, g and k are $\delta^{34}S$ values corresponding to the points in BSE images. The purple arrows emphasize the cycled variations of As and Au contents in the stage 2 and 3. (For interpretation of the references to color in this figure legend, the reader is referred to the web version of this article.)
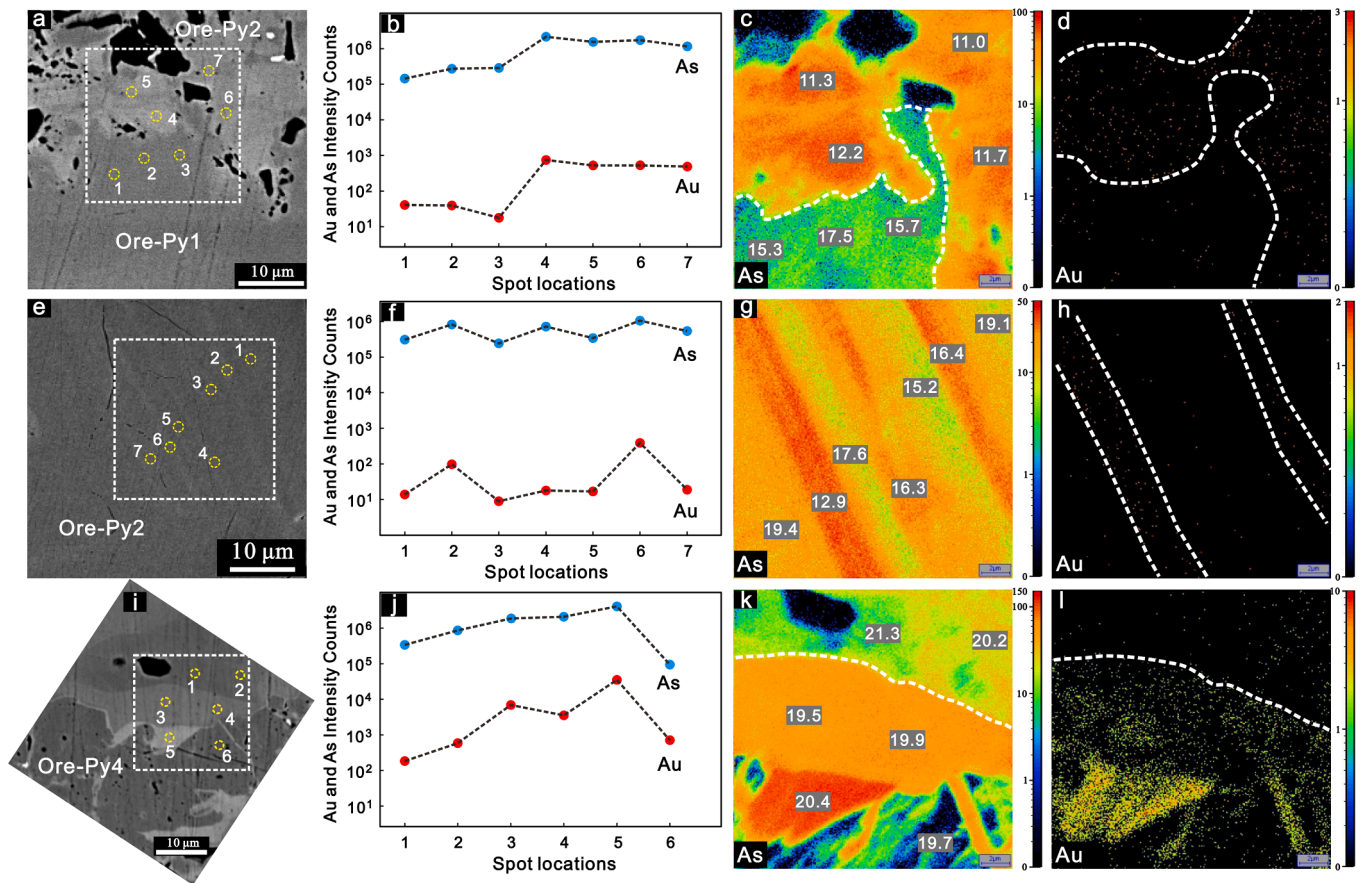
Fig. 8. Nano-SIMS elements mapping of representative Au-bearing pyrite from the Badu deposit. (a, e, i) BSE images of analyzed pyrite. The dashed boxes are areas of elements mapping. (b, f, j) Relative intensity counts of Au and As contents, which are contemporaneously obtained during sulfur isotope analyses. The points are labeled in BSE images. (c-d, g-h, k-l) Mappings of Au and As contents. The numbers in c, g and k are $\delta^{34}S$ values corresponding to the points in BSE images. The distribution of Au show positive correlations with that of As.
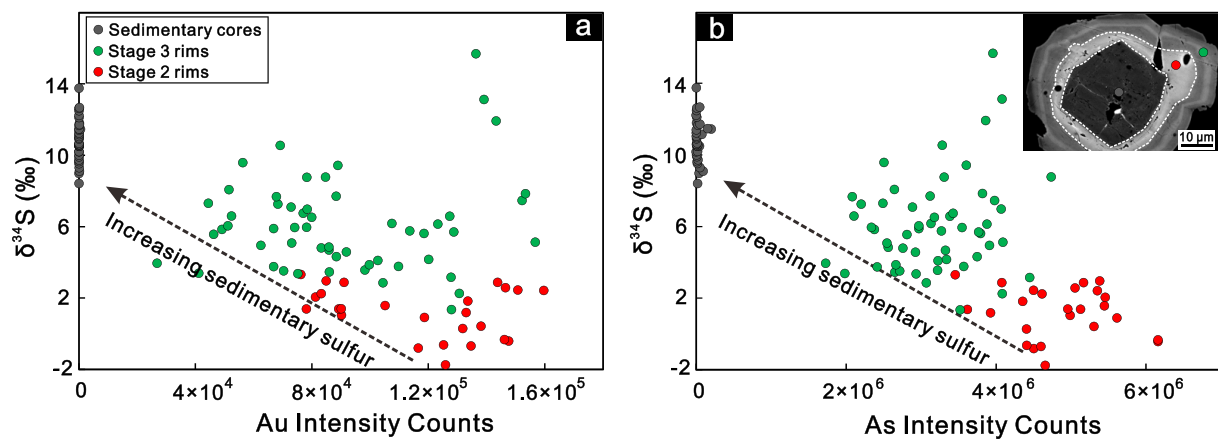

Fig. 9. Correlations of Au intensity counts with $\delta^{34}S$ values (a) and As intensity counts with $\delta^{34}S$ values (b) of Au-bearing pyrite from the Linwang deposit. The $\delta^{34}S$ values vary inversely with Au and As concentrations.

+10.8‰. Ore-Py1$_L$ yielded various $\delta^{34}S$ values of −1.7‰ to +15.7‰, which vary inversely with Au and As concentrations (Figs. 9-10). Among them, the stage 1 with elevated As and Cu and low Au contents has $\delta^{34}S$ values of +1.5‰ to +9.5‰, with an average of +5.1‰. The stage 2 with the highest As and Au contents yielded a narrow range of $\delta^{34}S$ values from −1.7‰ to +3.3‰, with an average of +1.2‰. The range of $\delta^{34}S$ values obtained in the stage 3 is +1.3‰ to +15.7‰, with an average of +7.1‰. In addition, $\delta^{34}S$ values in the stage 3 gradually increased

outwards and approached those of Pre-Py1$_L$ (Fig. 9).

For Badu, Pre-Py$_B$ yielded $\delta^{34}S$ values of −4.3‰ to −1.2‰. In contrast, Au-bearing grains are all characterized by highly positive $\delta^{34}S$ values ranging from +9.0‰ to +25.8‰, with an average of +18.1‰ (Fig. 10). Approximately 85 percent of these $\delta^{34}S$ values are between +15‰ and +22‰, with a median of +18.2‰. The inclusion-rich Ore-Py1$_B$ has lower $\delta^{34}S$ values of +9.0‰ to +14.2‰, with an average of +11.6‰. Ore-Py2$_B$ yielded $\delta^{34}S$ values of +12.9‰ to +20.3‰, with an
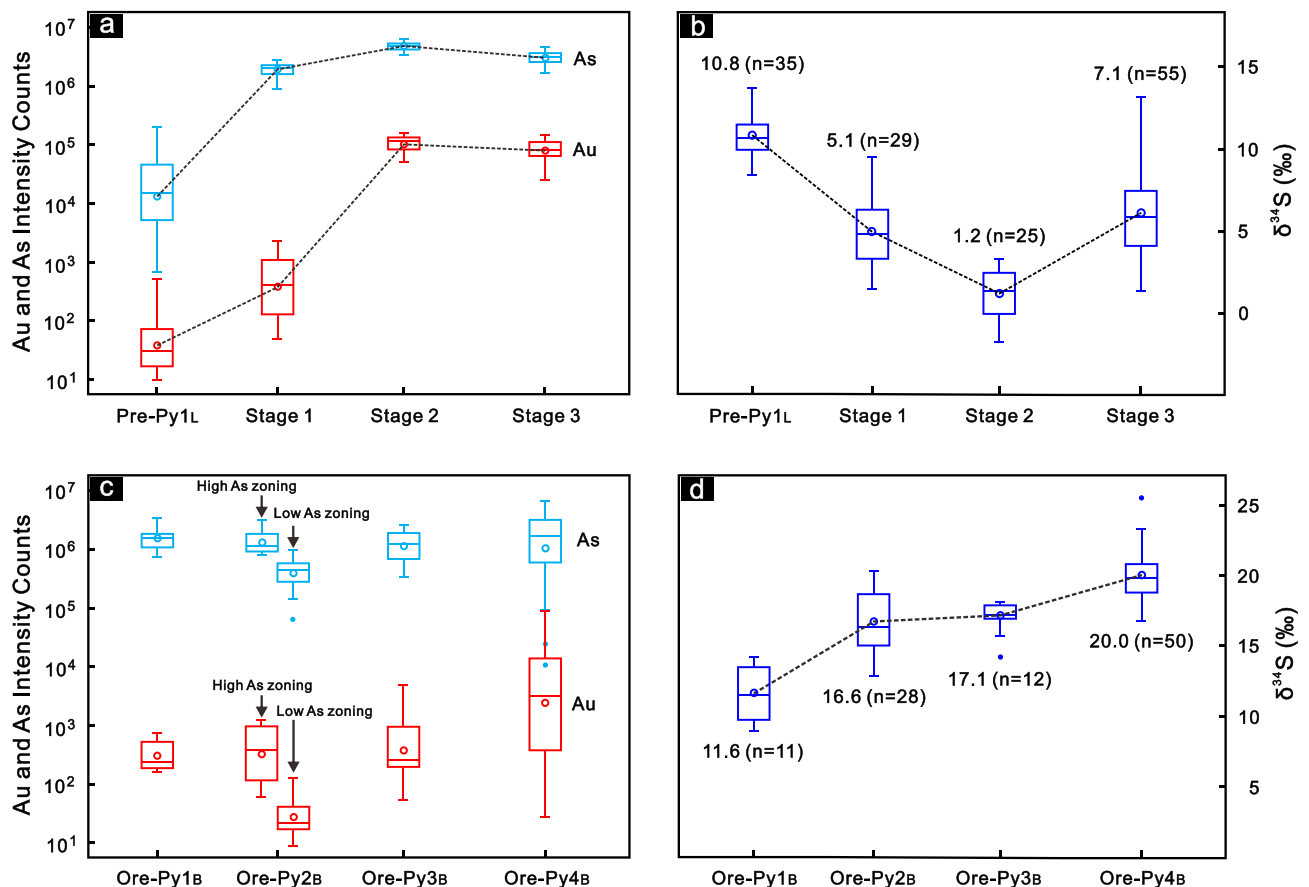
Fig. 10. Box diagrams of relative intensity counts of Au and As (a, c) and corresponding $\delta^{34}S$ values (b, d) of various pyrite types in the Linwang and Badu deposits, respectively.

average of +16.7‰, which are similar to those of Ore-Py3$_B$ ($\delta^{34}S$ = +14.2‰ to +19.4‰, average = +17.1‰). Ore-Py4$_B$ displays relatively higher $\delta^{34}S$ values of +16.7‰ to +25.8‰, with an average of +20.0‰. Additionally, large grain-scale variations in the $\delta^{34}S$ values for individual pyrite grain are also noticeable. For example, one pyrite grain yielded a $\delta^{34}S$ value of +9.3‰ in Ore-Py1$_B$ and then shows a progressive increase to +20.3‰ in Ore-Py2$_B$.

5. Discussion

5.1. Pyrite paragenesis

At Linwang, the sharp contacts, disparate chemical compositions, and dramatic changes in $\delta^{34}S$ values between the pyrite cores and rims, suggest that they formed during two discrete events, resembling those of Carlin-type gold deposits in Nevada (Gopon et al., 2020). The dark cores overgrown by Au-bearing rims are similar to Pre-Py1$_L$ observed in the barren samples and contain very low As and undetectable Au contents, suggesting that they formed at the pre-ore stage. Petrographic data show that Pre-Py1$_L$ is anhedral to euhedral and locally encloses sedimentary framboidal pyrite. Additionally, it contains abundant mineral inclusions of the surrounding clastic matrix and exhibits equilibrium textures with primary Fe-bearing dolomite. Thus, it is likely that Pre-Py1$_L$ formed during diagenesis or early hydrothermal event. In contrast, pyrite rims and individual fine-grained pyrite grains (Ore-Py1$_L$ and Ore-Py2$_L$) show intimate spatial and genetic relationships with decarbonation and silicification, both of which are important alterations related to Carlin-type Au mineralization (Cline et al., 2005; Su et al., 2009). Thus, we suggest that they are genetically related to Au mineralization and formed via sulfidation. This is further supported by their substantially

elevated As, Au, and Cu contents.

At Badu, Ore-Py1$_B$ to Ore-Py4$_B$ are not observed in fresh dolerite that only has minor Pre-Py$_B$ associated with magmatic iron–titanium oxides. Nano-SIMS mapping reveals that Ore-Py1$_B$ to Ore-Py4$_B$ belong to 'arsenic' pyrite and contain 'invisible' Au, suggesting that they formed during Au mineralization. Petrographic data show that hydrothermal alterations related to pyrite formation and Au mineralization occurred as following. During the incipient stage of alteration, the primary magmatic minerals were altered to ankerite, sericite, and rutile. Thereafter, pyrite preferentially replaced the newly formed ankerite. The early formed alteration minerals were enclosed in pyrite, forming the inclusion-rich Ore-Py1$_B$. As the replacement of ankerite proceeded, ore-forming fluids became progressively saturated with Fe, and pyrite was able to directly crystallize in open spaces, forming the clean Ore-Py2$_B$. Thus, Ore-Py1$_B$ and Ore-Py2$_B$ formed penecontemporaneously from successive evolutionary episodes of fluid flow. After primary pyrite crystals formed, they underwent dynamic recrystallization and hydrothermal modification via a coupled dissolution and reprecipitation (CDR) mechanism driven by a new infiltrating fluid during late deformation (Gao et al., 2022, submitted for publication.), forming Ore-Py3$_B$ and Ore-Py4$_B$, respectively.

5.2. Source and evolution of reduced sulfur in auriferous fluids

Au-bearing pyrites from the Linwang and Badu deposits show distinct micro-textures, metal associations and concentrations, and sulfur isotope compositions ($\delta^{34}S$ values). In particular, the variation in $\delta^{34}S$ values and its relationship with metals across Au-bearing pyrite rims at Linwang recorded the evolution of reduced sulfur in the auriferous fluids during mineralization processes, allowing the sulfur source

of the initial auriferous fluids to be constrained.

In the Youjiang Basin, CTGDs formed from acidic to nearly neutral, low f_{O2} and H_2S-dominated fluids, at temperatures of 180 to 245 ℃ (Su et al., 2009). Pyrite was the predominant sulfide. Very few sulfate minerals were formed during the final stage of hydrothermal systems. The sulfur isotope fractionation between pyrite precipitation and aqueous H_2S of fluids under these conditions is approximately 1‰ – 2‰ $[\Delta(\delta^{34}S_{pyrite} -\delta^{34}S_{fluids})] = +1‰$ to $+2‰$ (Ohmoto, 1972; Seal, 2006). Therefore, the measured $\delta^{34}S$ values of pyrite are approximately equal to those of the ore-forming fluids at the time pyrite precipitated from fluids (Ohmoto and Goldhaber,1997). However, the sulfur isotope composition of hydrothermal fluids can be influenced by changes in physico-chemical parameters (e.g., temperature, pH, and f_{O2}) and sulfur sources during mineralization (Seal, 2006). Decreasing the temperature of ore-forming fluids from 250 to 180 ℃ causes $\delta^{34}S$ variation of less than 1‰ (Ohmoto and Rye, 1979). The dissolution of Fe-bearing dolomite, stable formation of Fe-poor dolomite, and sericite-illite alteration during Au mineralization, suggest that the ore-forming fluids of Linwang and Badu were weakly acidic to nearly neutral with limited pH change (Xie et al., 2018), which should not result in significant $\delta^{34}S$ variation. Additionally, significant oxidation (f_{O2} fluctuation) of ore-forming fluids during mineralization, which could markedly modify the $\delta^{34}S$ values of fluids and precipitate pyrite with negative $\delta^{34}S$ values (Palin and Xu, 2000; Evans et al. 2006; Hodkiewicz et al., 2009; Peterson and Mavrogenes. 2014; LaFlamme et al., 2018; Wu et al., 2019), did not occur in Linwang or Badu. Petrographic data also suggest that sulfidation of host rocks, rather than fluid oxidation and boiling, is the trigger for Au deposition. This means that the temporal change in sulfur sources and fluid-rock interactions are the two most likely key factors affecting the $\delta^{34}S$ values of auriferous fluids.

5.3. Linwang deposit

The stage 1 of Au-bearing rims at the Linwang contains undetectable Au contents, suggesting that the early fluids were depleted in Au. The highest As and Au contents in the stage 2 are indicative of the injection of As- and Au-rich ore-forming fluids since this stage, representing the beginning of Au mineralization. The Au-rich fluids yielded the lowest $\delta^{34}S$ values of $-1.7‰$ to $+3.3‰$. Thereafter, the As and Au contents in the stage 3 gradually decreased owing to the consumption and dilution of metals in the ore-forming fluids. Correspondingly, the fluids in this stage recorded a wide range of $\delta^{34}S$ values that gradually increased towards the outer rims and approached those of the pre-ore pyrite ($\delta^{34}S = +8.4‰$ to $+13.8‰$) in the host rocks. From the inner to outer rims, the lack of sharp boundaries, continuity and overlap of $\delta^{34}S$ values, and affinities of trace elements indicate that the rims formed from evolving fluids. Some pyrite grains recorded a new injection of As- and Au-rich fluids, which initiated another cycle of As and Au variations. However, the magnitude of the new Au-rich fluids was much weaker than the former one, as shown by the unrecovered $\delta^{34}S$ values and lower metal contents.

Therefore, the coupled changes in $\delta^{34}S$ values and Au contents across the Au-bearing pyrite rims probably reflect two-endmembers mixing of reduced sulfur between the initial Au-rich ore-forming fluids with low $\delta^{34}S$ values and the Au-poor host rock with high $\delta^{34}S$ values (Fig. 9, Kesler et al., 2005; LaFlamme et al., 2018). The growth zoning recorded the variation in relative contributions of the two endmembers during Au mineralization. In the stage 2, reduced sulfur in the hydrothermal systems was dominated by that of the injected auriferous fluids. Whereafter, contributions of the host rock-derived ^{34}S-enriched sulfur gradually increased due to fluid-rock interaction and sedimentary sulfur assimilation during the stage 3. The injection of new Au- and As-rich fluids slightly renewed the $\delta^{34}S$ values of the fluids at that time, further suggesting that the auriferous fluids had $\delta^{34}S$ values that were distinct from those of sedimentary host. However, the secondary fluid incursion in the stage 3 was weak, and sedimentary sulfur remained

dominant.

The above discussion means that the $\delta^{34}S$ values ($-1.7‰$ to $+3.3‰$) of the stage 2 pyrite rims are most likely to represent the sulfur isotopic composition of the initial auriferous fluids, which are significantly distinct from those of sedimentary host strata. There are two plausible explanations for such narrow range and low $\delta^{34}S$ values: (1) reduced sulfur in the initial Au- and As-rich ore-forming fluids was originated from deep magmatic-hydrothermal endmembers that have $\delta^{34}S$ values of 0‰ to $+5‰$ (Seal, 2006); (2) sulfur was derived from deep, older, and currently unidentified sedimentary units (basement rocks) with average $\delta^{34}S$ values mirroring those of stage 2 pyrite. The deep stratigraphy of the Youjiang basin is dominated by *meso-* to NeoProterozoic volcanic-sedimentary and magmatic rocks (Hu et al., 2020b), whose sulfur isotopic compositions are currently unknown. Considering these unknowns, it is difficult to conclusively argue for a purely magmatic-hydrothermal origin for the reduced sulfur. However, recent geochronological studies revealed that there may exist igneous activities that were coeval with Au mineralization within and around the Youjiang basin (Li et al., 2013; Zhu et al., 2016; Gao, 2018; Su et al., 2021), which favored a possible genetic link between unrecognized deep magmatic-hydrothermal systems and Carlin-type Au mineralization in the Youjiang Basin.

5.4. Badu deposit

Au-bearing pyrites from the Badu deposit are characterized by highly positive $\delta^{34}S$ values varying from $+9.0‰$ to $+25.8‰$, with average of $+18.1‰$, which are by far the highest reported for Au-bearing pyrite of CTGDs in the Youjiang basin. Such $\delta^{34}S$ values are markedly distinct from those of magmatic sulfur reservoirs and the pre-existing fine-grained pyrite associated with primary magmatic minerals in fresh rocks.

Field observations have shown that the mineralized dolerite is spatially associated with the Devonian sedimentary rocks (Gao et al., 2021). Coincidentally, the positive $\delta^{34}S$ values of H_2S in the ore-forming fluids from Badu are comparable to those of diagenetic pyrite in the Devonian strata in the Youjiang basin ($\delta^{34}S= +11.7‰$ to $+37.6‰$, mainly concentrating in range of $+11.7‰$ to $+28‰$, Hou et al., 2016; Yan et al., 2020). These diagenetic pyrites are suggested to be formed through thermochemical sulfate reduction (TSR) processes during deep burial diagenesis (Qiu et al., 2018; Yan et al., 2020). Previous researches revealed that quantitative consumption and reduction of sulfate in a relatively closed system with a limited sulfate supply, such as euxinic water columns in restricted basins, could result in reduced sulfur with highly positive $\delta^{34}S$ values close to those of the sulfate source (Machel et al., 1995; Meshoulam et al., 2016; Qiu et al., 2018; Yan et al., 2020). In this condition, the resultant diagenetic pyrite in the Devonian strata could yield highly positive $\delta^{34}S$ values, with some values exceeding those of contemporaneous Devonian seawater sulfate ($\delta^{34}S= +16‰$ to $+23‰$; Kampschulte and Strauss, 2004; Fike et al., 2015). This mechanism has been also used to explain the high $\delta^{34}S$ values of SEDEX Pb-Zn deposits hosted within Devonian strata in the Youjiang basin (up to $+31‰$, Chen and Gao, 1988; Zeng and Liu, 1999; Chen et al., 2013; Qiu et al., 2018). Therefore, it is reasonably argued that H_2S in the ore-forming fluids of Badu was dominated by sedimentary sulfur derived from the Devonian strata.

CO_2-rich fluid inclusions, oxygen isotope data from hydrothermal quartz, and low Au concentrations in dolerite and sedimentary strata are suggestive of a deep origin for the ore-forming fluids of Badu (Dong, 2017; Li, 2020; Gao et al., 2021). Collectively, we propose that the initial auriferous fluids of Badu were originated from deep crust, migrated through the Devonian strata, and leached the sulfur with highly positive $\delta^{34}S$ values from the Devonian strata. Contamination of the sedimentary sulfur erased the primary sulfur isotopic signals of the initial auriferous fluids. Then, the evolved ore-forming fluids were transported into fractured dolerite, where they interacted with Fe-bearing minerals and

precipitated Au-bearing pyrite with high δ^{34}S values.

5.5. Comparation with other CTGDs in the Youjiang Basin

We compiled and reviewed approximately 1100 *in-situ* sulfur isotope data reported on Au-bearing pyrite from 11 CTGDs within the Youjiang Basin, aiming to reconcile their differences at a regional scale. Taking the Shuiyindong, Jinfeng, and Jinya deposits as representative examples, our own petrographic observation shows that Au-bearing pyrite grains from these deposits are composed of pre-ore-stage low-As dark porous cores (Pre-Py) and ore-stage high-As oscillatory-zoned rims (Ore-Py) (Fig. 11). These observations are comparable to previous studies, e. g., Xie et al. (2018) and Li et al. (2020) for Shuiyindong, Yan et al. (2018) for Jinfeng, and Wu. (2018) and Li et al. (2021) for Jinya. Pre-ore pyrite cores of Jinya are characterized by sieved textures and irregular and flexuose boundaries with Au-bearing pyrite rims, indicative of dissolution that is infilled and overgrown by Au-bearing pyrite (Fig. 11e).
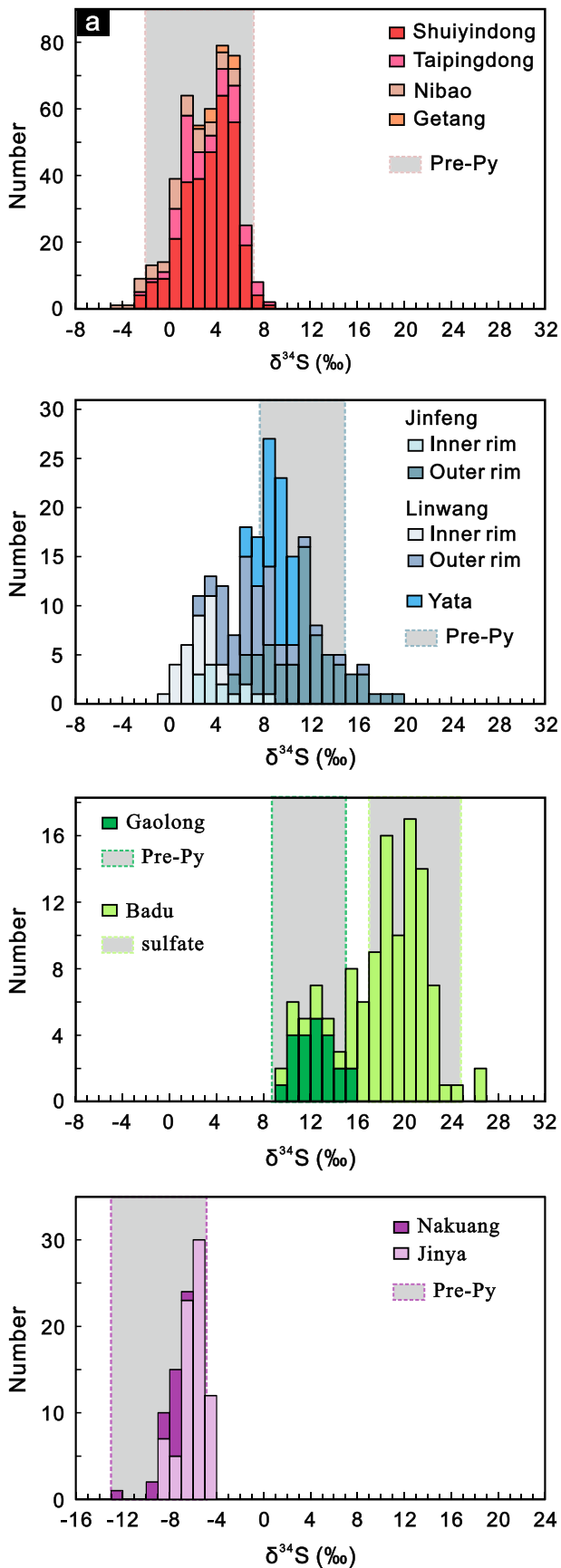
As illustrated in Fig. 12, the δ^{34}S values of Au-bearing pyrite rims in CTGDs in the Youjiang Basin display distinct spatial variations, which overlap with, and are dependent on, those of pre-ore pyrite in the sedimentary hosts. In detail, δ^{34}S values of Au-bearing pyrite rims from

those hosted by the Permian bioclastic limestone in the northwest of the basin (e.g., Shuiyindong, Taipingdong and Nibao) are concentrated in a narrow range of −3‰ to +5‰, with an average of +2.2‰. Gold-bearing rims from Gaolong-Badu and Jinya-Nakuang in the southeast of the basin display positive and negative δ^{34}S values, respectively (average of +11.5‰ for Gaolong, +18.1‰ for Badu, −5.5‰ for Jinya, and −8.2‰ for Nakuang). The δ^{34}S values of Au-bearing rims from Jinfeng and Linwang, located at the transitional zone, exhibit bimodal distributions of 0‰ to +5‰ and +7‰ to +15‰, respectively.

Such sediment host-dependent variations of δ^{34}S values of Au-bearing pyrite suggest that sedimentary sulfur has substantially contributed to the ore-forming systems during Au mineralization. Very low metamorphism of the sedimentary host (Suo et al., 1998), extremely low Au content in pre-ore pyrite (Xie et al.,2018), and the lack of transition of pyrite to pyrrhotite are inconsistent with a metamorphic devolatilization model (Pitcairn et al., 2006; Large et al., 2011; Thomas et al., 2011). In contrast, an external As- and Au-rich fluid are required for Au mineralization. Therefore, sulfur contributions from sedimentary host rocks were mainly achieved by direct dissolution and leaching of pre-ore sulfur-bearing phases. Irregular boundaries and corroded textures are indicative of the dissolution of pre-ore pyrite during mineralization. Phase equilibrium relationships also suggest that the formation
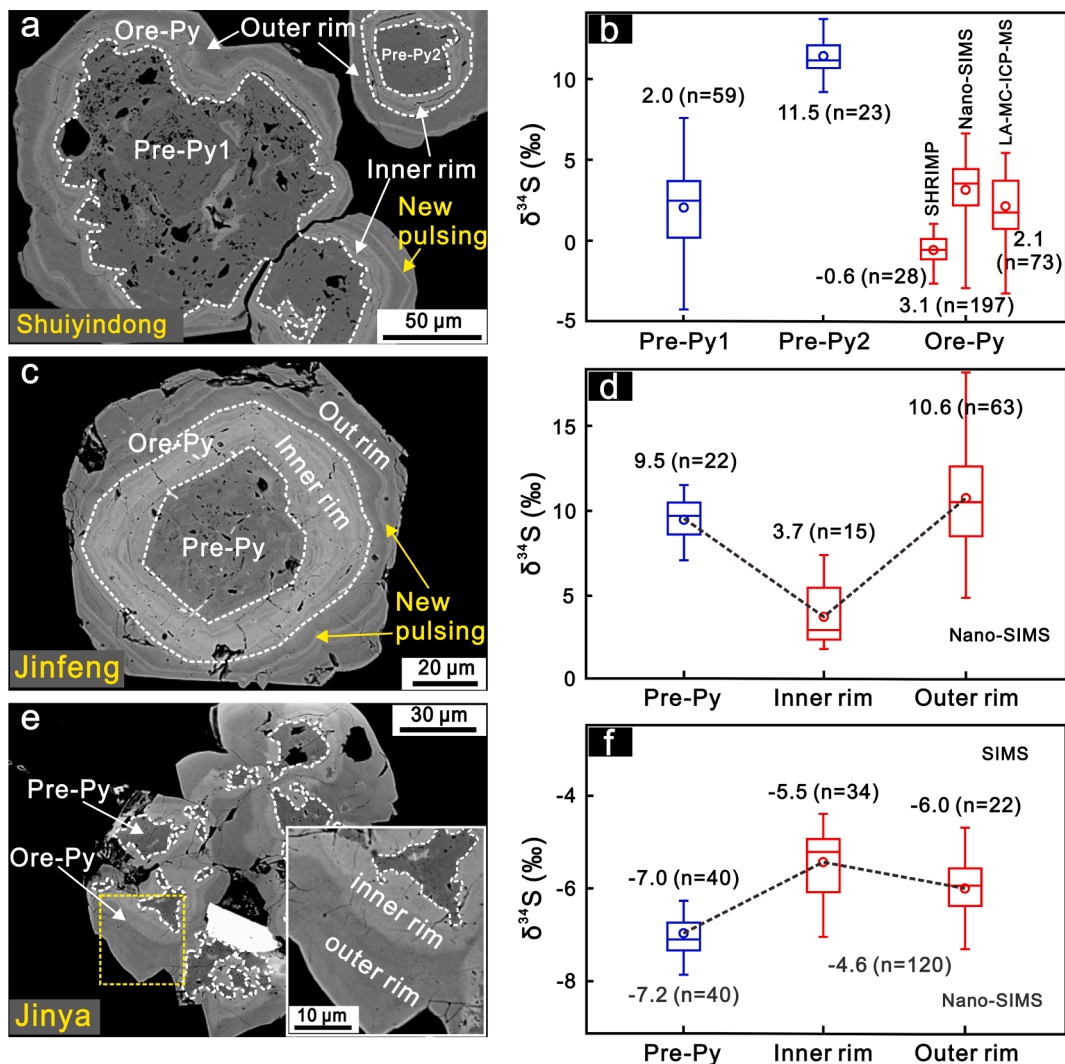
Fig. 11. BSE images (a, c, e) and δ^{34}S values (b, d, f) of representative pyrite grains from the Shuiyindong, Jinfeng and Jinya deposits in the Youjiang Basin, respectively. All pyrite grains are composed of pre-ore cores (Pre-Py) and Au-bearing rims (Ore-Py). δ^{34}S values of the Shuiyindong include those obtained by SHRIMP (Hou et al., 2016), Nano-SIMS (Li et al., 2020), and LA-MC-ICP-MS analyses (Jin, 2017; Xie et al., 2018). The δ^{34}S data of Jinfeng and Jiya were from Yan et al. (2018) and Li et al. (2021), respectively.

of late realgar and orpiment requires an increase in the f_{S2} of ore-forming fluids with decreasing temperatures, indicating that considerable sedimentary sulfur must have been added to the initial auriferous fluids (Hofstra and Cline, 2000; Kesler et al., 2005).

The variation in δ³⁴S values and its relationship with Au contents across Au-bearing pyrite rims from the Linwang deposit suggest that the highly variable δ³⁴S values of Au-bearing pyrites from different deposits in the basin result from the interactions between the initial auriferous fluids of deep magmatic-hydrothermal origin and the sedimentary hosts with different δ³⁴S signatures. It should be noted that the vast majority of previously compiled sulfur isotope data were mainly obtained via LA-MC-ICP-MS analyses using large beam sizes, which yielded mixed values for Au-bearing pyrite rims with multiple growth zones. For examples, high-resolution Nano-SIMS analyses show that the inner and outer parts of the Au-bearing pyrite rims from the Jinfeng have δ³⁴S values of +1.1‰ to +7.9‰ and +4.9‰ to +18.1‰, respectively (Fig. 10d, Yan et al., 2018). However, the LA-MC-ICP-MS data yielded mixed values of +8.9‰ to +11.2‰ (Xie et al., 2018). In Jinya, SIMS and Nano-SIMS data show that δ³⁴S values of the inner rims with high As and Au contents are clearly shifted towards an endmember with near-zero δ³⁴S values compared with those of pre-ore cores (Fig. 10f), which is inconsistent with fault-value models that will reduce the δ³⁴S values of Au-bearing pyrite (Peterson and Mavrogenes, 2014). The outer rims have δ³⁴S values gradually approaching those of pre-ore pyrite (Li, 2019; Li et al., 2021), indicating contribution of sulfur from the sedimentary host.

Collectively, we propose that reduced sulfur in the initial ore-forming fluids of CTGDs in the Youjiang Basin was primarily originated from deep magmatic-hydrothermal systems, and that substantial contaminations of sedimentary host-derived sulfur during mineralization resulted in the spatially variable δ³⁴S signatures recorded in Au-bearing pyrites. Strikingly, δ³⁴S data imply that magmatic signals of the initial auriferous fluids gradually decreased from the northwest to the southeast of the basin.

6. Conclusions

The variation in sulfur isotope composition and its relationship with metal concentrations across Au-bearing pyrite can be used to constrain the source and evolution of reduced sulfur in the ore-forming fluids of Carlin-type gold deposits (CTGDs). High-resolution Nano-SIMS sulfur isotope analysis and elemental mapping of Au-bearing pyrite with complex zoning suggest that the reduced sulfur in the initial Au- and As-rich ore-forming fluids of CTGDs in the Youjiang Basin was originated from deep magmatic-hydrothermal systems. Strong fluid-rock interactions and host rock-derived sulfur contributions could have erased primary sulfur isotope information and resulted in highly variable and sedimentary host-dependent sulfur isotope compositions of Au-bearing pyrites, which may account for the controversial interpretations of the ultimate source of reduced sulfur that transports Au in ore-forming fluids.

Declaration of Competing Interest

The authors declare that they have no known competing financial interests or personal relationships that could have appeared to influence the work reported in this paper.

(caption on next column)

Acknowledgements

Appendix A. Supplementary data

Supplementary data to this article can be found online at https://doi.org/10.1016/j.oregeorev.2022.104990.

References

Barker, S.L., Hickey, K.A., Cline, J.S., Dipple, G.M., Kilburn, M.R., Vaughan, J.R., Longo, A.A., 2009. Uncloaking invisible gold: use of NanoSIMS to evaluate gold, trace elements, and sulfur isotopes in pyrite from Carlin-type gold deposits. Econ. Geol. 104, 897–904.

Bureau of Geology and Mineral Resources of GuangXi Province (BGMRGX), 1992. Magmatic rocks in the Baduxu district: 1: 50000 regional geological survey report for Baduxu district (G-48-140-B). Guilin, the People's Republic of China. 119-143.

Cai, J.X., Zhang, K.J., 2009. A new model for the Indochina and South China collision during the Late Permian to the Middle Triassic. Tectonophysics 467, 35–43.

Chen, D.Z., Wang, J.G., Racki, G., Li, H., Wang, C.Y., Ma, X.P., Whalen, M.T., 2013. Large sulfur isotopic perturbations and oceanic changes during the Frasnian-Famennian transition of the Late Devonian. J. Geol. Soc. Lond. 170, 465–476.

Chen, M.H., Huang, Q.W., Li, J.X., Jiang, B.C., Zhang, C.M., 2010. Structure analysis and structural metallogenies of the Linwang gold deposit, Leye, Guangxi. China. Geotect. et Metall. 34, 349–361 in Chinese with English abstract.

Chen, X.P., Gao, J.Y., 1988. Thermal water deposition and Pb-Zn Barite deposits in the Devonian system, central Guangxi. Chin. J. Geochem. 7, 321–328.

Cheng, Y.B., Mao, J.W., Xie, G.Q., Chen, M.H., Yang, Z.X., 2009. Zircon U-Pb dating of granite in Gejiu super-large tin polymetallic orefield and its significance. Miner. Deposits 28, 297–312.

Cheng, Y.B., Mao, J.W., Chen, X.L., Li, W., 2010. LA-ICP-MS Zircon U-Pb Dating of the Bozhushan granite in Southeastern Yunnan province and its significance. J. Jilin Univ. 40, 869–878 in Chinese with English abstract.

Cline, J.S., Hofstra, A.H., 2000. Ore fluid evolution at the Getchell Carlin- type gold deposit, Nevada, USA. Europ. J. Miner. 12, 195–212.

Cline, J.S., Hofstra, A.H., Muntean, J.L., Tosdal, R.M., Hickey, K.A., 2005. Carlin-type gold deposits in Nevada, Critical geologic characteristics and viable models. Econ. Geol. 451–484, 100th anniversary.

Cline, J.S., Muntean, J.L., Gu, X.X., Xia, Y., 2013. A comparison of Carlin-type gold deposits: Guizhou Province, golden triangle, Southwest China, and northern Nevada. USA. Ear. Sci. Fro. 20, 1–18.

Cline, J.S., 2018. Nevada's Carlin-Type gold deposits, what we've learned during the past 10 to 15 years. Society of Economic Geologists, Inc. Reviews in Economic Geology, Diversity of Carlin-type gold deposits 20, 7–37.

Dong, W.D., 2017. Geochemistry of dolerite-hosted gold deposit along the southern margin of Youjiang basin. Unpublished Ph.D dissertation, Guiyang, China, Institute of Geochemistry, Chinese Academy of Sciences (in Chinese with English abstract).

Du, Y.S., Huang, H.W., Huang, Z.Q., Xu, Y.J., Yang, J.H., Huang, H., 2009. Basin translation from Late Paleozoic to Triassic of Youjiang basin and its tectonic signification. Geo. Sci. Tech. Info. 28, 10–15 in Chinese with English abstract.

Du, Y.S., Huang, H., Yang, J.H., Huang, H.W., Tao, P., Huang, Z.Q., Hu, L.S., Xie, C.X., 2013. The basin translation from Late Paleozoic to Triassic of the Youjiang basin and its tectonic signification. Geo. Rev. 59, 1–11 in Chinese with English abstract.

Emsbo, P., Hutchinson, R.W., Hofstra, A.H., Volk, J.A., Bettles, K.H., Baschuk, G.J., Johnson, C.A., 1999. Syngenetic Au on the Carlin trend: Implications for Carlin-type deposits. Geology 27, 59–62.

Emsbo, P., Hofstra, A.H., 2003. Origin and significance of postore dissolution collapse breccias cemented with calcite and barite at the Meikle gold deposit, northern Carlin trend. Nevada. Econ. Geol. 98, 1243–1252.

Evans, K.A., Phillips, G.N., Powell, R., 2006. Rock-Buffering of Auriferous Fluids in Altered Rocks Associated with the Golden Mile-Style Mineralization, Kalgoorlie Gold Field, Western Australia. Econ. Geol. 101, 805–817.

Feng, J.R., Mao, J.W., Pei, R.F., Zhou, Z.H., Yang, Z.X., 2010. SHRIMP zircon U-Pb dating and geochemical characteristics of Laojunshan granite intrusion from the Wazha tungsten deposit, Yunnan province and their implications for petrogenesis. Acta Petrol. Sin. 26, 845–857 in Chinese with English abstract.

Fike, D.A., Bradley, A.S., Rose, C.V., 2015. Rethinking the ancient sulfur cycle. Ann. Rev. Earth Planet. Sci. 43, 593–622.

Gao, W., 2018. Geochronology and Geodynamics of Carlin-type gold deposit in the Youjiang basin (NW Guangxi). Unpublished Ph.D dissertation, Guiyang, China, Institute of Geochemistry, Chinese Academy of Sciences (in Chinese with English abstract).

Gao, W., Hu, R.Z., Hofstra, A.H., Li, Q.L., Zhu, J.J., Peng, K.Q., Mu, L., Huang, Y., Ma, J. W., Zhao, Q., 2021. U-Pb dating on hydrothermal rutile and monazite from the badu gold deposit supports an early cretaceous age for carlin-type gold mineralization in the Youjiang Basin, Southwestern China. Econ. Geol. 116, 1355–1385.

Gao, W., Hu, R.Z, Mei, L., Bi, X.W., 2022. Micro-textures and trace elements of Au-bearing pyrite of the Badu deposit in the Youjiang Basin, SW China: implications for high-grade gold mineralization. Am. Miner. Submitted for publication.

Gopon, P., Douglas, J.O., Auger, M.A., Hansen, L., Wade, J., Cline, J.S., Robb, L.J., Moddy, M.P., 2020. A nanoscale investigation of Carlin-type gold deposits: an atom-scale elemental and isotopic perspective. Econ. Geol. 114, 1123–1133.

Gu, X.X., Zhang, Y.M., Li, B.H., Dong, S.Y., Xue, C.J., Fu, S.H., 2012. Hydrocarbon and ore-bearing basinal fluids: a possible link between gold mineralization and hydrocarbon accumulation in the Youjiang basin. South China. Miner. Deposita 47, 663–682.

Hodkiewicz, P.F., Groves, D.I., Davidson, G.J., Weinberg, R.F., Hagemann, S.G., 2009. Influence of structural setting on sulphur isotopes in Archean orogenic gold deposits, Eastern Goldfields Province, Yilgarn. Western Australia. Miner. Deposita 44, 129–150.

Hofstra, A.H., Snee, L.W., Rye, R.O., Folger, H.W., Phinisey, J.D., Loranger, R.J., Dahl, A. R., Naeser, C.W., Stein, H.J., Lewchuk, M., 1999. Age constraints on Jerritt Canyon and other Carlin-type gold deposits in the western United States-relationship to Mid-Tertiary extension and magmatism. Econ. Geol. 94, 769–802.

Hofstra, A.H., Cline, J.S., 2000. Characteristics and models for Carlin-type gold deposits. Rev. in Econ. Geol. 13, 163–220.

Hou, L., Peng, H.J., Ding, J., Zhang, J.R., Zhu, S., Wu, S., Wu, Y., Ouyang, H.G., 2016. Textures and In Situ Chemical and Isotopic Analyses of Pyrite, Huijiabao Trend, Youjiang Basin, China: Implications for Paragenesis and Source of Sulfur. Econ. Geol. 111, 331–353.

Hu, R.Z., Su, W.C., Bi, X.W., Tu, G.Z., Hofstra, A.H., 2002. Geology and geochemistry of Carlin-type gold deposits in China. Miner. Deposita 37, 378–392.

Hu, R.Z., Zhou, M.F., 2012. Multiple Mesozoic mineralization events in South China-an introduction to the thematic issue. Miner. Deposita 47, 579–588.

Hu, R.Z., Fu, S.L., Huang, Y., Zhou, M.F., Fu, S.H., Zhao, C.H., Wang, Y.J., Bi, X.W., Xiao, J.F., 2017. The giant South China Mesozoic low-temperature metallogenic domain, Reviews and a new geodynamic model. J. Asian Earth Sci. 137, 9–34.

Hu, R.Z., Wen, H.J., Ye, L., Chen, W.T., Xia, Y., Fan, H.F., Huang, Y., Zhu, J.J., Fu, S.L., 2020a. Metallogeny of critical metals in the Southwestern Yangtze Block. Chin. Sci. Bull. 65, 3700–3714 in Chinese with English abstract.

Hu, R.Z., Chen, W., Bi, X.W., Fu, S.L., Yin, R.S., Xiao, J.F., 2020b. Control of the Precambrian basement on the formation of the Mesozoic largescale low-temperature mineralization in the Yangtze Craton. Ear. Sci. Fro. 27, 137–150 in Chinese with English abstract.

Hu, X.L., Gong, Y.J., Zeng, G.P., Zhang, Z.J., Wang, J., Yao, S.Z., 2018. Multistage pyrite in the Getang sediment-hosted disseminated gold deposit, southwestern Guizhou Province, China: Insights from textures and in situ chemical and sulfur isotopic analyses. Ore Geol. Rev. 99, 1–16.

Jinfeng Corporation, 2018. Topographic and geological map of Baduxu gold-antimony ore district, Tianlin country, Guangxi province. Unpublished internal exploration report of the Badu gold deposit, Guangxi, China. 376.

Jin, X.Y., 2017. Geology, mineralization and genesis of the Nibao, Shuiyindong and Yata gold deposit in SW Guizhou province, China. University of Geosciences (in Chinese with English abstract), Wuhan, China, China. Published Ph.D. dissertation.

Jin, X.Y., Hofstra, A.H., Hunt, A.G., Liu, J.Z., Yang, W., Li, J.W., 2020. Noble gases fingerprint the source and evolution of ore-forming fluids of Carlin-type gold deposits in the golden triangle, South China. Econ. Geol. 115, 455–469.

Kampschulte, A., Strauss, H., 2004. The sulfur isotopic evolution of Phanerozoic seawater based on the analysis of structurally substituted sulfate in carbonates. Chem. Geol. 204, 255–286.

Kesler, S.E., Riciputi, L.C., Ye, Z.J., 2005. Evidence for a magmatic origin for Carlin-type gold deposits, Isotopic composition of sulfur in the Betze-Post-Screamer deposit, Nevada, USA. Miner. Deposita 40, 127–136.

LaFlamme, C., Sugiono, D., The'baud, N., Caruso, S., Fiorentini, M., Selvaraja, V., Jeon, H., Voute, F., Martin, L., 2018. Multiple sulfur isotopes monitor fluid evolution in an orogenic gold deposit. Geochim. Cosmochim. Acta 222, 436–446.

Large, R.R., Danyushevsky, L., Hollit, C., Maslennikov, V., Meffre, S., Gilbert, S., Bull, S., Scott, R., Embsbo, P., Thomas, H., Singh, B., Foster, J., 2009. Gold and trace element zonation in pyrite using a laser imaging technique: Implications for the timing of gold in orogenic and Carlin style sediment-hosted deposits. Econ. Geol. 104, 635–668.

Large, R.R., Bull, S.W., Maslennikov, V.V., 2011. A carbonaceous sedimentary source-rock model for Carlin-type and orogenic gold deposits. Econ. Geol. 106, 331–358.

Large, S.J.E., Bakker, E.Y.N., Weis, P., Walle, M., Heinrich, C.A., Ressel, M.W., 2016. Trace elements in fluid inclusions in sediment-hosted gold deposits: Indicators for a magmatic-hydrothermal origin for the Carlin and Battle Mountain ore trend. Geology 44, 1015–1018.

Li, J.K., Wang, D.H., Li, H.Q., Chen, Z.H., Mei, Y.P., 2013. Late Jurassic-Early Cretaceous mineralization in the Laojunshan ore concentration area. Yunnan province. J. Jilin Univ. 38, 1023–1036 in Chinese with English abstract.

Li, J.W., 2020. Micro-textures and geochemical characteristics of hydrothermal quartz from low-temperature gold and antimony deposits in the Youjiang basin, SW China: implications for the mineralization process. Unpublished Ph.D dissertation, Guiyang, China, Institute of Geochemistry, Chinese Academy of Sciences (in Chinese with English abstract).

Li, J.X., 2019. Study on the metallogenetic source and the fluid evolution of Carlin type gold deposits-a case study of in situ sulfur isotopes and trace elements of pyrites of gold deposits from two sedimentary facies in the Youjiang Basin. Unpublished Ph.D dissertation, Guiyang, China, Institute of Geochemistry, Chinese Academy of Sciences (in Chinese with English abstract).

Li, J.X., Zhao, C.H., Huang, Y., Zhuo, Y.Z., Li, J.W., 2019. In-situ sulfur isotope and trace element of pyrite constraints on the formation and evolution of the Nibao Carlin-type gold deposit in SW China. Acta Geochim 38, 555–575.

Li, J.X., Hu, R.Z., Zhao, C.H., Zhu, J.J., Huang, Y., Gao, W., Li, J.W., Zhuo, Y.Z., 2020. Sulfur isotope and trace element compositions of pyrite determined by NanoSIMS and LA-ICP-MS: new constraints on the genesis of the Shuiyindong Carlin-like gold deposit in SW China. Miner. Deposita 55, 1279–1298.

Li, X.H., Bai, L.A., Yue, Z.H., Pang, B.C., Wei, D.T., 2021. Mineralization processes involved in the formation of the Jinya Carlin-type Au deposit, northwestern Guangxi, China: Evidence from in situ trace element and S isotope geochemistry of Au-bearing zoned pyrite. Ore Geol. Rev. 138, 104376.

Liang, J.L., Li, J., Liu, X.M., Zhai, W., Huang, Y., Zhao, J., Sun, W.D., Song, M.C., Li, J.Z., 2020. Multiple element mapping and in-situ S isotopes of Au-carrying pyrite of Shuiyindong gold deposit, southwestern China using NanoSIMS: Constraints on Au sources, ore fluids, and mineralization processes. Ore Geol. Rev. 123, 103–576.

Machel, H.G., Krouse, H.R., Sassen, R., 1995. Products and distinguishing criteria of bacterial and thermochemical sulfate reduction. App. Geochem. 10, 373–389.

Meshoulam, A., Ellis, G.S., Ahmad, W.S., Deev, A., Sessions, A.L., Tang, Y.C., Adkins, J.F., Liu, J.Z., Gilhooly, W.P., Aizenshtat, Z., Amrani, A., 2016. Study of thermochemical sulfate reduction mechanism using compound specific sulfur isotope analysis. Geochim. Cosmochim. Acta 188, 73–92.

Metcalfe, I., 2006. Palaeozoic and Mesozoic tectonic evolution and palaeogeography of East Asian crustal fragments: The Korean Peninsula in context. Gondwana Res. 9, 24–46.

Muntean, J.L., Cline, J.S., Simon, A.C., Longo, A.A., 2011. Magmatic-hydrothermal origin of Nevada's Carlin-type gold deposits. Nat. Geo. 4, 122–127.

Muntean, J.L., Cline, J.S., 2018. Diversity of Carlin-type gold deposits. Society of Economic Geologists, Inc. Rev. Eco. Geol. Diver. Carlin-type Gold Deposits 20, 1–5.

Ohmoto, H., 1972. Systematics of sulfur and carbon isotopes in hydrothermal ore deposits. Econ. Geol. 67, 551–578.

Ohmoto, H., Rye, R.O., 1979. Isotopes of sulfur and carbon. In: Barnes, H.L. (Ed.), Geochemistry of Hydrothermal Ore Deposits: New York. Wiley, pp. 509–567.

Ohmoto, H., Goldhaber, M.B., 1997. Sulfur and carbon isotopes. In: Barnes, H.L. (Ed.), Geochemistry of Hydrothermal Ore Deposits, third ed. Wiley, pp. 517–611.

Palenik, C.S., Utsunomiya, S., Reich, M., Kesler, S.E., Wang, L.M., Ewing, R.C., 2004. "Invisible" gold revealed: direct imaging of gold nanoparticles in a Carlin-type deposit. Am. Mineral. 89, 1359–1366.

Palin, J.M., Xu, Y., 2000. Gilt by association? Origins of pyritic gold ores in the Victory mesothermal gold deposit, Western Australia. Econ. Geol. 95, 1627–1634.

Peterson, E.C., Mavrogenes, J.A., 2014. Linking high-grade gold mineralisation to earthquake-induced fault-valve processes in the Porgera gold deposit, Papua New Guinea. Geology 42, 383–386.

Pitcairn, I.K., Teagle, D.A.H., Craw, D., Olivo, G.R., Kerrich, R., Brewer, T.S., 2006. Sources of Metals and Fluids in Orogenic Gold Deposits: Insights from the Otago and Alpine Schists, New Zealand. Econ. Geol. 101, 1525–1546.

Pokrovski, G.S., Akinfiev, N.N., Borisova, A.Y., Zotov, A.V., Kouzmanov, K., 2014. Gold speciation and transport in geological fluids: insights from experiments and physical-chemical modelling. Geol. Soc. Lon. Special Pu. 402, 9–70.

Qin, K., 2018. Geochemical characteristics and mineralization of the Gaolong gold deposit in Guangxi. Published M.S. dissertation, Beijing, China, China University of Geosciences (in Chinese with English abstract).

Qiu, L., Yang, D.P., Tang, S.L., Wang, Q., Yang, W.X., Tang, X.L., Wang, J.B., 2016. Mesozoic geology of southwestern China: Indosinian foreland overthrusting and subsequent deformation. J. Asian Earth Sci. 122, 91–105.

Qiu, W.H.J., Zhou, M.F., Li, X., Williams-Jones, A.E., Yuan, H., 2018. The Genesis of the Giant Dajiangping SEDEX-Type Pyrite Deposit, South China. Econ. Geol. 113, 1419–1446.

Reich, M., Kesler, S.E., Utsunomiya, S., Palenik, C.S., Chryssoulis, S.L., Ewing, R.C., 2005. Solubility of gold in arsenian pyrite. Geochim. Cosmochim. Acta 69, 2781–2796.

Seal, R.R., 2006. Sulfur isotope geochemistry of sulfide minerals. Rev. Mineral. Geochem. 61, 633–677.

Simon, G., Kesler, S.E., Chryssoulis, S., 1999. Geochemistry and textures of gold-bearing arsenian pyrite, Twin Creeks, Nevada: Implications for deposition of gold in Carlin-type deposits. Econ. Geol. 94, 405–422.

Song, C.A., Feng, Z.H., Lei, L.Q., 2009. Geotectonic metallogenic evolution and belt of Tin polymetal ore and exploration in Guangxi. J. Guilin Univ. Tech. 29, 207–215 in Chinese with English abstract.

Su, H.M., Jiang, S.Y., Shao, J.B., Zhang, D.Y., Wu, X.K., Huang, X.Q., 2021. New identification and significance of Early Cretaceous mafic rocks in the interior South China Block. Sci. Rep. 11, 11396.

Su, W.C., Heinrich, C.A., Pettke, T., Zhang, X.C., Hu, R.Z., Xia, B., 2009. Sediment-hosted gold deposits in Guizhou, China, products of wall-rock sulfidation by deep crustal fluids. Econ. Geol. 104, 73–93.

Su, W.C., Zhang, H.T., Hu, R.Z., Ge, X., Xia, B., Chen, Y.Y., Zhu, C., 2012. Mineralogy and geochemistry of gold-bearing arsenian pyrite from the Shuiyindong Carlin-type gold deposit, Guizhou, China, implications for gold depositional processes. Miner. Deposita 47, 653–662.

Su, W.C., Dong, W.D., Zhang, X.C., Shen, N.P., Hu, R.Z., Hofstra, A.H., Cheng, L.Z., 2018. Carlin-type gold deposits in the Dian-Qian-Gui "Golden Triangle" of Southwest China. Society of Economic Geologists, Inc. Rev. Econ. Geol. Diversity Carlin-type Gold Deposits 20, 157–185.

Suo, S.T., Bi, X.M., Zhao, W.X., Hou, G.J., 1998. Very low-grade metamorphism and its geodynamical significance of Triassic strata within the Youjiang River basin. Sci. Geol. Sin. 33, 396–405 in Chinese with English abstract.

Thomas, H.V., Large, R.R., Bull, S.W., Maslennikov, V., Berry, R.F., Fraser, R., Froud, S., Moye, R., 2011. Pyrite and pyrrhotite textures and composition in sediments, laminated quartz veins, and reefs at Bendigo gold mine, Australia: insights for ore genesis. Econ. Geol. 106, 1–31.

Tosdal, R.M., Cline, J.S., Fanning, C.M., Wooden, J.L., 2003. Lead in the Getchell-Turquoise Ridge carlin-type gold deposits from the perspective of potential igneous and sedimentary rock sources in northern Nevada: Implications for fluid and metal Sources. Econ. Geol. 98, 1189–1211.

Wang, Y.J., Fan, W.M., Zhang, G.W., Zhang, Y.H., 2013. Phanerozoic tectonics of the South China Block: key observations and controversies. Gond. Res. 23, 1273–1305.

Wei, D.T., Xia, Y., Gregory, D.D., Steadman, J.A., Tan, Q.P., Xie, Z.J., Liu, X.J., 2020. Multistage pyrites in the Nibao disseminated gold deposit, southwestern Guizhou Province, China: Insights into the origin of Au from textures, in situ trace elements, and sulfur isotope analyses. Ore Geol. Rev. 122, 103446.

Williams-Jones, A.E., Bowell, R.J., Migdisov, A.A., 2009. Gold in solution. Elements 5, 281–287.

Wu, W., 2018. Mineralization of the Jinya and Nakuang Carlin-like gold deposits in Northwest Guangxi. Published M.S. dissertation, Beijing, China, China University of Geosciences (in Chinese with English abstract).

Wu, Y.F., Evans, K., Li, J.W., Fougerouse, D., Large, R.R., Guagliardo, P., 2019. Metal remobilization and ore-fluid perturbation during episodic replacement of auriferous pyrite from an epizonal orogenic gold deposit. Geochim. Cosmochim. Acta 245, 98–117.

Xie, Z.J., Xia, Y., Cline, J., Pribil, M.J., Koenig, A.E., Tan, Q.P., Wei, D.T., Wang, Z.P., Yan, J., 2018. Magmatic Origin for Sediment-Hosted Au Deposits, Guizhou Province, China. In Situ Chemistry and Sulfur Isotope Composition of Pyrites. Shuiyindong and Jinfeng Deposits. Econ. Geol. 113, 1625–1652.

Yan, D.P., Zhou, M.F., Wang, Y.C., Xia, B., 2006. Structural and geochronological constraints on the tectonic evolution of the Dulong-Song Chay tectonic dome in Yunnan province. SW China. J. Asian Earth Sci. 28, 332–353.

Yan, H., Pi, D.H., Jiang, S.Y., Hao, W.D., Cui, H., Robbins, L.J., Mänd, K., Li, L., Planavsky, N.J., Konhauser, K.O., 2020. Hydrothermally induced ^{34}S enrichment in pyrite as an alternative explanation of the Late-Devonian sulfur isotope excursion in South China. Geochim. Cosmochim. Acta 283, 1–21.

Yan, J., Hu, R.Z., Liu, S., Lin, Y.T., Zhang, J.C., Fu, S.L., 2018. Nano-SIMS element mapping and sulfur isotope analysis of Au-bearing pyrite from Lannigou Carlin-type Au deposit in SW China, new insights into the origin and evolution of Au-bearing fluids. Ore Geol. Rev. 92, 29–41.

Yang, J.H., Cawood, P.A., Du, Y.S., Huang, H., Hu, L.S., 2012. Detrital record of Indosinian mountain building in SW China: Provenance of the Middle Triassic turbidites in the Youjiang Basin. Tectonophysics 574–575, 105–117.

Zeng, Y.Y., Liu, T.B., 1999. Characteristics of the Devonian Xialei manganese deposit, Guangxi Zhuang Autonomous Region. China. Ore Geol. Rev. 15, 153–163.

Zhao, J., Liang, J.L., Li, J., Huang, Y.I., Liu, X., Zhang, J.C., Hao, J.L., Sun, W.D., Li, J.Z., Xie, J.Q., 2020. Gold and sulfur sources of the Taipingdong Carlin-type gold deposit: Constraints from simultaneous determination of sulfur isotopes and trace elements in pyrite using nanoscale secondary ion mass spectroscopy. Ore Geol. Rev. 117, 103–299.

Zhang, J.C., Lin, Y.T., Yang, W., Shen, W.J., Hao, J.L., Hu, S., Cao, M.J., 2014. Improved precision and spatial resolution of sulfur isotope analysis using NanoSIMS. J. Anal. Atom. Spectrom 29, 1934–1943.

Zhao, J.H., Zhou, M.F., Yan, D.P., Zheng, J.P., Li, J.W., 2011. Reappraisal of the ages of Neoproterozoic strata in South China: no connection with the Grenvillian orogeny. Geology 39, 299–302.

Zhu, J.J., Zhong, H., Xie, G.Q., Zhao, C.H., Xu, L.L., Lu, G., 2016. Origin and geological implication of the inherited zircon from felsic dykes, Youjiang basin. China. Acta Petrol. Sin. 32, 3269–3280 in Chinese with English abstract.